Myocardial Innervation

11

Markus Schwaiger, Arnold F. Jacobson, Antti Saraste,
Jagat Narula, and Frank M. Bengel

The heart is innervated by sympathetic and parasympathetic fibers of the autonomic nervous system (ANS). The ANS plays a critical role in modifying cardiac performance to respond quickly and effectively to changing demands on cardiovascular performance. The sympathetic nervous system, which has the highest density of nerve terminals in the right and left ventricles, is predominantly stimulatory, producing positive inotropic and chronotropic effects. In contrast, the parasympathetic nervous system, which exerts primarily negative chronotropic responses, has nerve fibers predominantly in the atria [1].

Two kinds of neurons, preganglionic and postganglionic, are involved in ANS signal transmission. Postganglionic neurons provide innervation to target organs and tissues via synapses between nerve terminals and receptors on the surface of end-organ cells. Signal transmission is mediated by neurotransmitters that are released into the synapse from the nerve terminal and bind with postsynaptic receptors to initiate the effector response. After the signal transmission is completed, the neurotransmitter is released back into the synapse, from where it typically diffuses into nonneuronal tissue or the circulation (unchanged or after metabolism/catabolism), or it is actively returned to the nerve terminal via transporter proteins on presynaptic cell surfaces.

The predominant sympathetic neurotransmitter is norepinephrine (NE), which is synthesized, stored, and metabolized within the sympathetic nerve terminal. Upon neurostimulation, the neurotransmitter is released by exocytosis into the synaptic cleft. A small portion of the released neurotransmitter interacts with post-synaptic α- and β-adrenergic receptors, predominantly β-1 receptors in the heart. The majority of the released neurotransmitter undergoes reuptake in the nerve terminals (uptake 1) by means of the NE transporter (a sodium/chloride-dependent transport protein), which has a high affinity for amines (catecholamines and catecholamine analogues). Inside the nerve terminal, NE is either metabolized by monoamine oxidase or sequestered in vesicles by the vesicular monoamine transporter, a proton-dependent transport protein localized in the vesicle membrane. The amine transport system (uptake 1) regulates the extraneuronal concentration of androgenic neurotransmitters and plays an important physiologic and pathophysiologic role in modifying signal transduction and extraneuronal catecholamine concentration. This regulatory role includes the reuptake of locally released norepinephrine as well as the uptake and metabolism of circulating catecholamines that enter the extracellular space. This high-affinity uptake system protects the heart from the deleterious effects of elevated levels of circulating catecholamines [2, 3].

M. Schwaiger
Department of Nuclear Medicine,
Technical University of Munich, Munich, Germany

A. F. Jacobson (✉)
Diagram Consulting, Kihei, HI, USA

A. Saraste
Turku PET Centre, Turku University Hospital and University
of Turku, Turko, Finland

J. Narula
Icahn School of Medicine at Mount Sinai, New York, NY, USA

F. M. Bengel
Department of Nuclear Medicine, Hannover Medical School,
Hannover, Germany

V. Dilsizian, J. Narula (eds.), *Atlas of Nuclear Cardiology*, https://doi.org/10.1007/978-3-030-49885-6_11

The predominant parasympathetic neurotransmitter is acetylcholine, which is synthesized and stored within the parasympathetic nerve terminal. Comparable to sympathetic neurons, stimulation results in neurotransmitter release by exocytosis. The predominant receptor in the heart is the M_2 muscarinic receptor, which is present in much higher density in the atria than in the ventricles. Subsequent to neurostimulation of these receptors, the action of acetylcholine is terminated by the enzyme acetylcholinesterase in the synapse, which degrades the neurotransmitter to choline and acetate. These inactive molecules are then reabsorbed into the presynaptic terminal and used to synthesize new acetylcholine.

The importance of the myocardial autonomic nervous system is magnified in patients with heart disease, as damage to one or both branches can result in imbalances that increase the risk for adverse outcomes such as heart failure progression and arrhythmic events [4, 5]. The status of the ANS also influences the effects and effectiveness of cardiac medications and interventions. These factors have led to efforts to develop imaging agents for examining this system and quantifying the deleterious effects of various heart diseases. The greatest efforts and successes have been achieved with agents specific for presynaptic and postsynaptic sympathetic neuronal targets.

The remainder of this chapter provides an overview of the tracers, both single-photon and positron emitting, and nuclear-imaging methodologies used to study sympathetic innervation of the heart, as well as their clinical applications. It is hoped that future research will provide equivalent insights and applications for imaging of the parasympathetic nervous system of the heart.

Autonomic Nervous System

Figures 11.1, 11.2, and 11.3 illustrate the structure of the ANS, its control mechanisms, and the mechanisms controlling neurotransmitter synthesis and release.

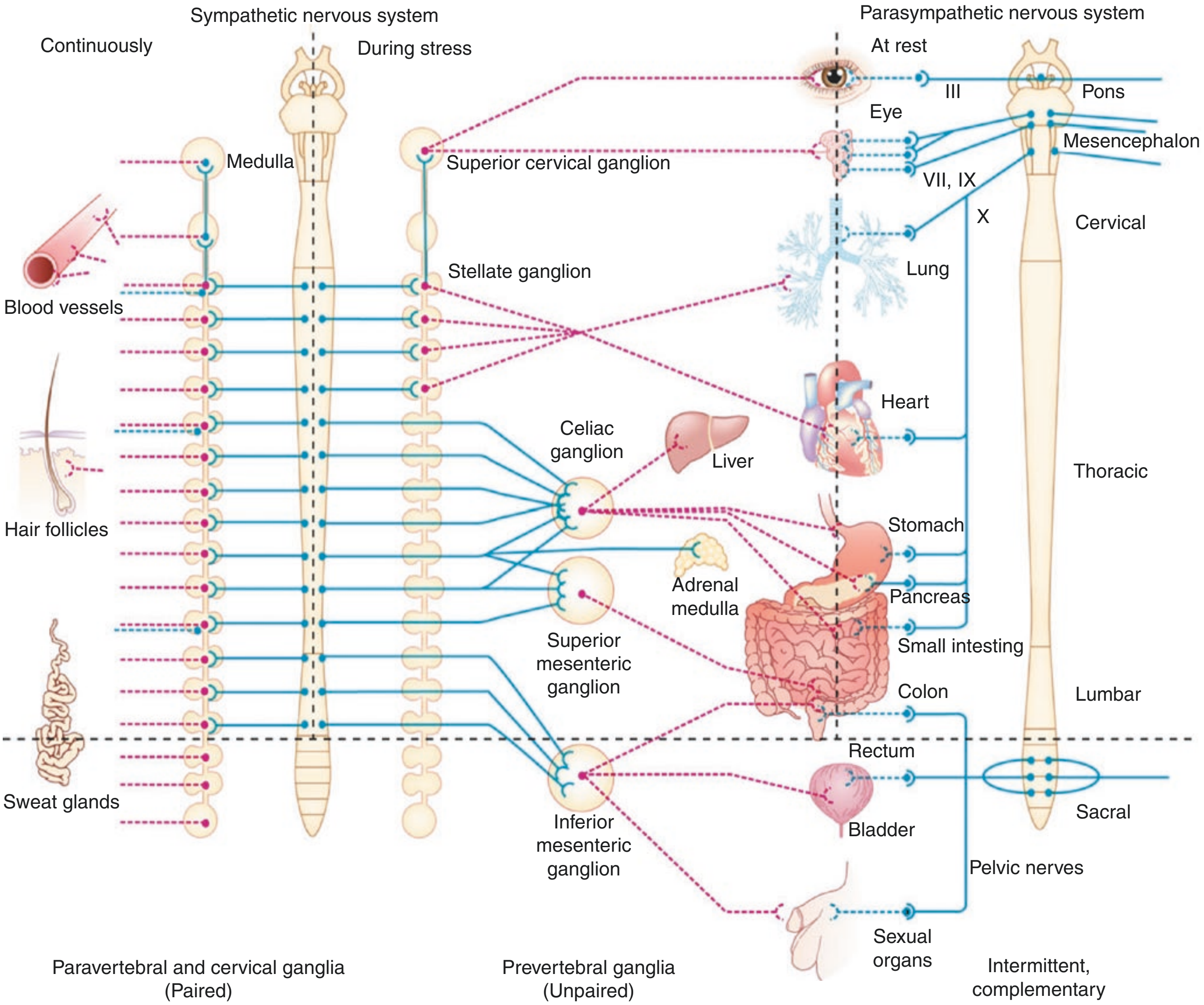

Fig. 11.1 Structure of the autonomic nervous system (ANS). The ANS is historically divided into two major efferent components, the sympathetic nervous system (cervicothoracic, SNS) and parasympathetic nervous system (craniosacral, PNS). In either case, end-organ innervation is provided by nerve fibers originating from autonomic ganglia located outside the central nervous system (CNS), which is driven by preganglionic cholinergic input from the CNS (*solid blue lines*). The main differences consist of the types of principal transmitter used by the postganglionic fibers (PNS: acetylcholine [*dotted blue lines*]; SNS: norepinephrine [*dotted red lines*]), the location of the ganglia (PNS: near or within the end organs; SNS: near the spinal cord, either paravertebral [22 pairs] or prevertebral [unpaired]), the degree of divergence and convergence of preganglionic input to postganglionic neurons (PNS: very little; SNS: considerable), and their respective functional roles. Most internal organs receive input from both the PNS and SNS (*center*). Important exceptions include skin and blood vessel (pilomotor and sudomotor) functions, which are exclusively controlled by noradrenergic and cholinergic postganglionic fibers of SNS origin only (*left*), and the adrenal gland, which functions as the equivalent of a sympathetic ganglion, causing systemic catecholamine release (80% epinephrine, 20% norepinephrine) in response to preganglionic cholinergic stimulation. In the case of most internal organs, the SNS and PNS exert opposite effects. PNS effects normally prevail at rest, whereas SNS effects predominate during stress or exercise (“flight or fight” response). In genitourinary organs, SNS and PNS functions are complementary; for example, PNS mediates erection and SNS mediates ejaculation [6]

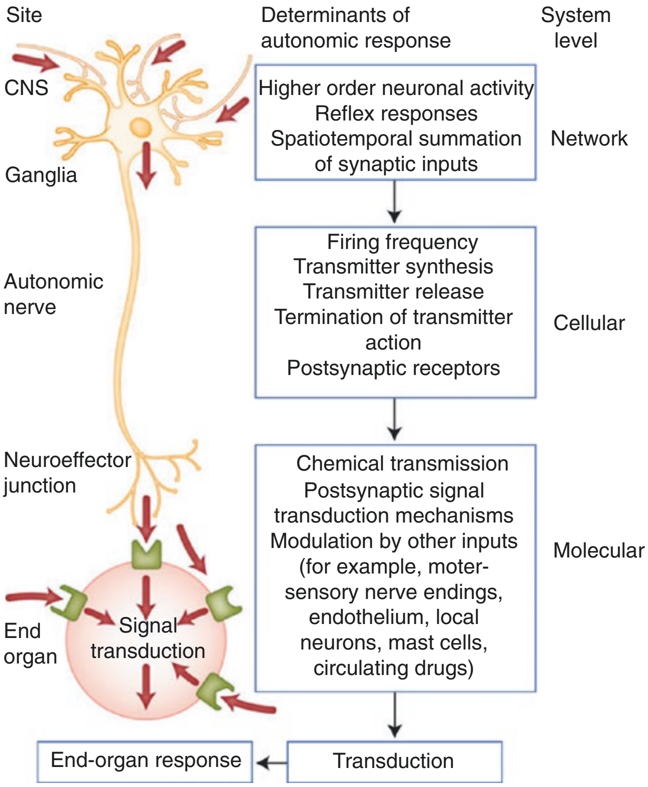

Fig. 11.2 Determinants of end-organ control by the autonomic nervous system. Control mechanisms operate concurrently at different system levels. At a neural network level, the processing and integration of patterns of neuronal activity (including reflex responses) determine the firing frequency of autonomic efferent nerve fibers. Cellular mechanisms that are operative at the level of nerve terminals determine the types, amounts, and fates of chemical transmitters released at autonomic synapses and neuroeffector junctions. At a molecular level, the membrane receptor and postsynaptic signal transduction mechanisms determine the types and magnitude of cellular effector responses. At each of these system levels, various interactions occur between distinct functional divisions of the ANS (sympathetic, parasympathetic, afferent, enteric, and local neuronal systems) involving classic (cholinergic and adrenergic) transmitters as well as a variety of nonclassic neurotransmitter systems. CNS- central nervous system [7]

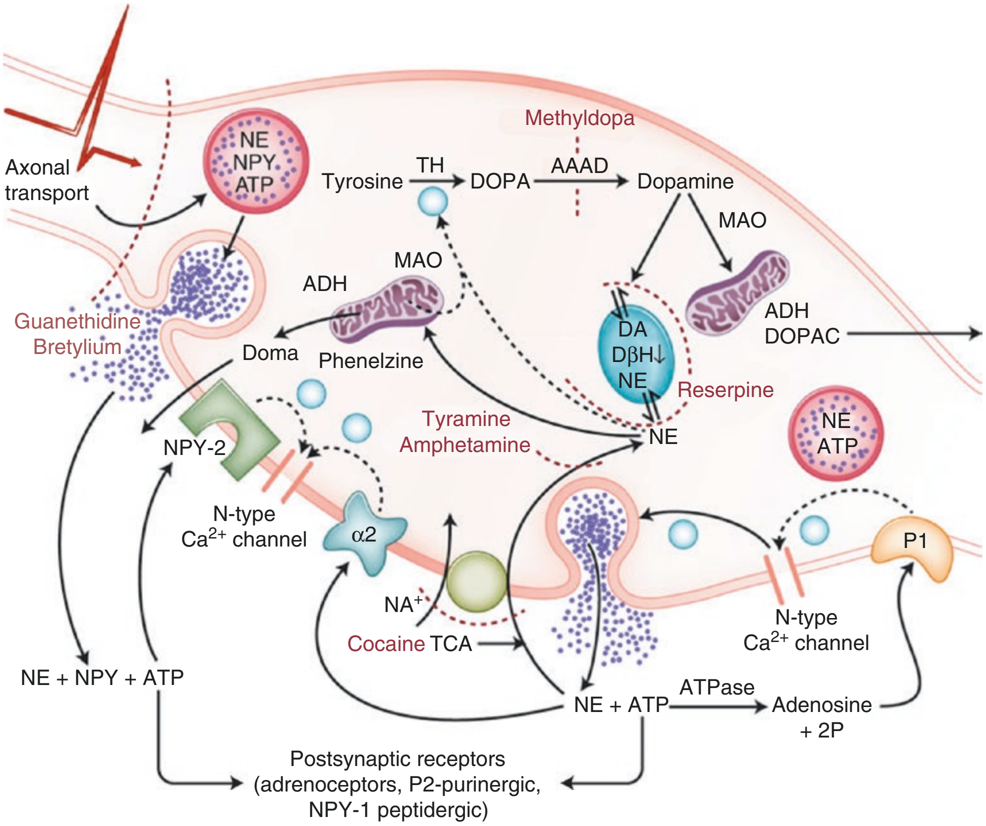

Fig. 11.3 Neurotransmitter synthesis and release at adrenergic nerve terminals. Mechanisms controlling transmitter synthesis and release at adrenergic nerve terminals are shown. Transmitters are stored in two types of synaptic vesicles: small vesicles containing only the principal transmitter norepinephrine (NE) and cotransmitter adenosine triphosphate (ATP) (each is synthesized within the nerve terminal itself) and larger, dense-core vesicles containing the polypeptide cotransmitter neuropeptide Y (NPY) and chromogranin (both of which are exclusively synthesized in the cell soma) as well as NE and ATP. The rate-limiting step for NE synthesis in the nerve terminal is tyrosine hydroxylase (TH) enzyme activity, which is negatively controlled by the cytoplasmic concentration of NE. The TH enzymatic product DOPA is decarboxylated to dopamine by (unspecific) aromatic L-amino acid decarboxylase (AAAD) in a step subject to therapeutic interference by provision of the "false" substrate methyldopa (resulting in the eventual formation of the "false transmitter" methyl-NE). Dopamine is to equal proportions either deaminated and excreted as 3,4-dihydroxyphenylacetic acid (DOPAC) or taken up into dopamine-β-hydroxylase (DβH)–containing storage vesicles via a reserpine-sensitive active uptake process and hydroxylated to NE. The cytoplasmic concentration of NE is determined by a dynamic equilibrium established between diffusion (leakage) out of storage vesicles, reserpine-sensitive (active) reuptake into storage vesicles, cytoplasmic displacement and extrusion by indirect sympathomimetics such as tyramine and amphetamine, reuptake from the extracellular space via a Na$^+$-dependent cotransport mechanism sensitive to inhibition by cocaine or tricyclic antidepressants (TCAs), and elimination after metabolizing to 3,4-dihydroxymandelic acid (Doma) by mitochondrial monoamine oxidase (MAO) and aldehyde dehydrogenase (ADH), a pathway sensitive to inhibition by MAO inhibitors such as phenelzine. In adrenal medullary neurons, 80% of cytoplasmic NE is methylized by *N*-methyltransferase into epinephrine before being packaged into storage vesicles. The nerve stimulation-evoked physiologic transmitter release occurs via fusion of synaptic storage vesicles with the cell membrane after the invasion of the nerve terminal by propagated action potentials (sensitive to blockade by guanethidine or bretylium) and the resulting increase in cytoplasmic Ca^{2+} through activation of voltage-sensitive (predominantly N-type) Ca^{2+} channels. Upon release, ATP, NE, and NPY produce neuroeffector responses through actions on postsynaptic membrane receptors. In addition, all three transmitters inhibit further release through action on presynaptic (P1, 2-adrenergic, NPY-2) receptors [8, 9]. Transmitter actions are terminated by hydrolysis (ATP), reuptake into nerve terminals (NE), uptake into nonneuronal tissue, and metabolism by catechol-*O*-methyltransferase (COMT) (NE), and diffusion away from the terminal and into the bloodstream (NE, NPY) [10]

Radiotracers

Several radiolabeled compounds have been synthesized to probe the sympathetic nervous system at the presynaptic and postsynaptic levels [11]. These tracers can be divided into radiolabeled catecholamines and catecholamine analogues. The most commonly employed single-photon emission CT (SPECT) tracer is metaiodobenzylguanidine (*m*IBG), which represents an analogue of the antihypertensive drug guanethidine [12]. Radiolabeled catecholamine analogues for positron emission tomography (PET) include metaminol, metahydroxyephedrine, and phenylephrine [13–15]. These "false adrenergic neurotransmitters" share the same reuptake mechanism and endogenous storage with the true neurotransmitters, but they are not metabolized and display a decreased affinity for postsynaptic receptor proteins.

As a functional analogue of NE, the uptake of *m*IBG occurs in all neuronal tissues that express the energy-dependent NE transporter (T) system (uptake-1). Although passive diffusion of [^{123}I]*m*IBG also occurs into nonneuronal cells (uptake-2), for the quantities of [^{123}I]*m*IBG used for diagnostic imaging, cellular uptake via the norepinephrine transporter (NET) system dominates.

Myocardial imaging with [^{123}I]*m*IBG has historically involved two imaging sessions, one early (15–30 minutes post-injection) and one late (3–4 hours post-injection). At both times, planar and SPECT imaging can be performed, depending on the methods that are being employed for quantitation. Quantitation of myocardial uptake is usually done in terms of the heart/mediastinum ratio (H/M or HMR) of counts/pixel values. HMR can be calculated from regions of interest drawn on anterior planar images of the thorax or from comparable volumes of interest on SPECT studies. Myocardial activity in early images reflects primarily the integrity of NET function, whereas activity in late images is affected by levels of *m*IBG storage in vesicles (mediated by vesicular monoamine transporter 2 [VMAT2]) and sympathetic neuronal stimulation controlling rates of NE and *m*IBG release [16–22]. Global and regional quantitation of [^{123}I]*m*IBG uptake, as a measure of sympathetic neuronal integrity, is most commonly based on late images. The difference between uptake in early and late images, designated "washout," is often considered an index of sympathetic nervous system activation. Quantitative assessments of both neuronal uptake and washout have been demonstrated to reflect the severity of cardiac disease and the prognosis for subsequent adverse events [23].

The most successful PET radiopharmaceutical agent for the imaging of presynaptic function is C-11 hydroxyephedrine (^{11}C-HED) [24, 25]; ^{11}C-HED is produced by the N-methylation of metaraminol using C-11 methyl iodide (Fig. 11.4). In contrast to *m*IBG, uptake of this tracer primarily reflects the transport by NET. Vesicle storage seems to occur, but binding inside the vesicle is weaker than with norepinephrine, owing to its higher lipid solubility. Based on experimental observations, myocardial retention reflects a continuing release and reuptake of ^{11}C-HED in the nerve terminal. Tracer retention is commonly quantified by calculating the retention index or retention fraction (which reflects the myocardial activity at 40 minutes), normalized to the integral of the arterial input function [18]. More recently, a tracer kinetic model for ^{11}C-HED kinetics has been developed, which allows calculation of the distribution volume within the myocardium.

As an alternative PET tracer to ^{11}C-HED, C-11 epinephrine has been proposed as a naturally occurring transmitter. Myocardial retention of this tracer represents the uptake, metabolism, and storage of catecholamines [26].

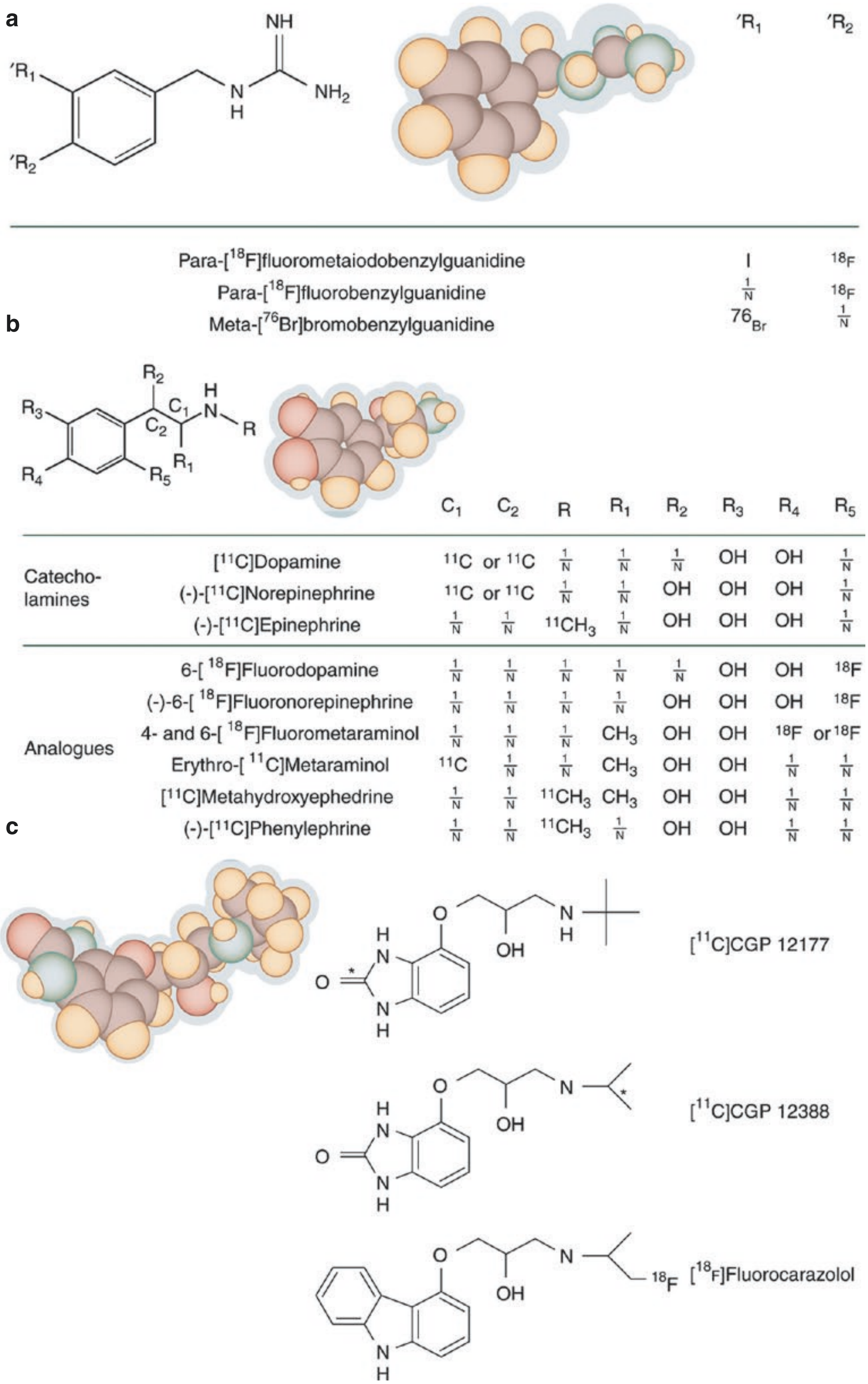

	'R1	'R2
Para-[^{18}F]fluorometaiodobenzylguanidine	I	^{18}F
Para-[^{18}F]fluorobenzylguanidine	H	^{18}F
Meta-[^{76}Br]bromobenzylguanidine	^{76}Br	H

		C_1	C_2	R	R_1	R_2	R_3	R_4	R_5
Catecholamines	[^{11}C]Dopamine	^{11}C or	^{11}C	H	H	H	OH	OH	H
	(-)-[^{11}C]Norepinephrine	^{11}C or	^{11}C	H	H	OH	OH	OH	H
	(-)-[^{11}C]Epinephrine	H	H	$^{11}CH_3$	H	OH	OH	OH	H
Analogues	6-[^{18}F]Fluorodopamine	H	H	H	H	H	OH	OH	^{18}F
	(-)-6-[^{18}F]Fluoronorepinephrine	H	H	H	H	OH	OH	OH	^{18}F
	4- and 6-[^{18}F]Fluorometaraminol	H	H	H	CH_3	OH	OH	^{18}F or	^{18}F
	Erythro-[^{11}C]Metaraminol	^{11}C	H	H	CH_3	OH	OH	H	H
	[^{11}C]Metahydroxyephedrine	H	H	$^{11}CH_3$	CH_3	OH	OH	H	H
	(-)-[^{11}C]Phenylephrine	H	H	$^{11}CH_3$	H	OH	OH	H	H

Fig. 11.4 Positron emission tomography (PET) radiotracers for mapping of cardiac sympathetic neurons. The radiotracers used for the evaluation of the sympathetic nervous system can be classified into three categories: radiolabeled analogues of benzylguanidine (**a**), radiolabeled catecholamines or catecholamine analogues (**b**), and β-adrenoceptor ligands (**c**). The common lead structure and a computed model of the prototypic compounds are provided. The ^{11}C-carbon position in panel *a* is indicated by $'R_1$ and $'R_2$ and in panel *b* by C_1 and C_2. The radiolabeled compounds are listed under the lead structures and computed models

Normal Myocardial Innervation

Figures 11.5, 11.6, 11.7, 11.8 and 11.9 demonstrate tracer activity in normal myocardium.

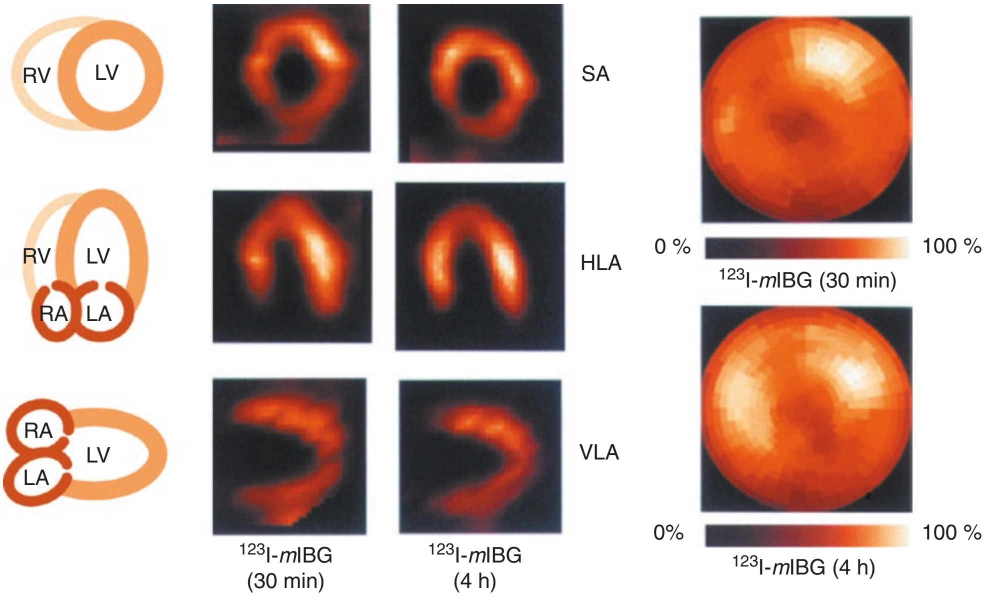

Fig. 11.5 I-123 metaiodobenzylguanidine (^{123}I-*m*IBG) distribution in normal myocardium. These single-photon emission CT (SPECT) images were obtained in a healthy volunteer 30 minutes and 4 hours after an intravenous injection of 10 mCi ^{123}I-*m*IBG. Regional myocardial tracer retention is displayed in the short-axis (SA), horizontal long-axis (HLA), and vertical long-axis (VLA) views. There is a homogeneous uptake of the tracer throughout the myocardium of the left ventricle (LV). The right ventricle (RV), right atrium (RA), and left atrium (LA) are not seen because of their thin walls. Polar maps represent the three-dimensional distribution of the tracer within the LV. The activity at the apex is displayed at the center of the map, whereas the basal parts of the LV represent the outer rings. The activity is normalized to maximal activity within the LV. The regional tracer retention was determined by the circumferential radial search for activity maxima. The individual circumferential profiles of several myocardial slices are then combined into one representative polar map. On both 30-minute and 4-hour images, there is relatively lower ^{123}I-*m*IBG activity in the inferior and inferoseptal areas, consistent with the known heterogeneity of neuronal distribution [4, 5]. The normal washout rate between early and late images is typically in the 5–20% range, whereas HF patients commonly have rates as high as 30–50% [19]. The late images are considered specific for the relative distribution of sympathetic nerve terminals, whereas washout has been used as a marker of neuronal integrity or sympathetic tone

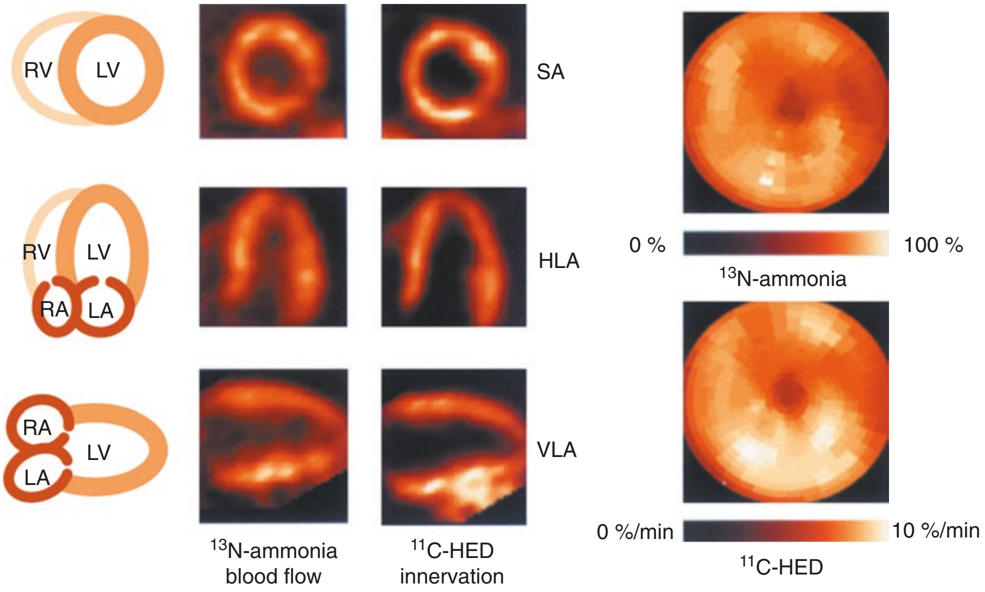

Fig. 11.6 C-11 hydroxyephedrine (^{11}C-HED) distribution in normal myocardium. These PET images in short-axis (SA), horizontal long-axis (HLA), and vertical long-axis (VLA) views were obtained following an injection of 20 mCi ^{13}N-ammonia as a blood flow marker and about 40 minutes after the intravenous injection of 20 mCi ^{11}C-HED. The myocardial blood flow is homogeneous throughout the left ventricle (LV), paralleled by the homogeneous uptake of ^{11}C-HED in all segments of the LV. Polar maps using a circumferential profile analysis display homogeneous distribution of ^{13}N-ammonia and ^{11}C-HED. The polar maps of flow are normalized to their own maxima, whereas the ^{11}C-HED data are expressed by retention index. This index represents the activity at 40 minutes normalized to arterial input function, derived from a region of interest placed over LV activity. These dynamic PET images allow for generation of myocardial and blood time–activity curves. LA left atrium, RA right atrium, RV right ventricle

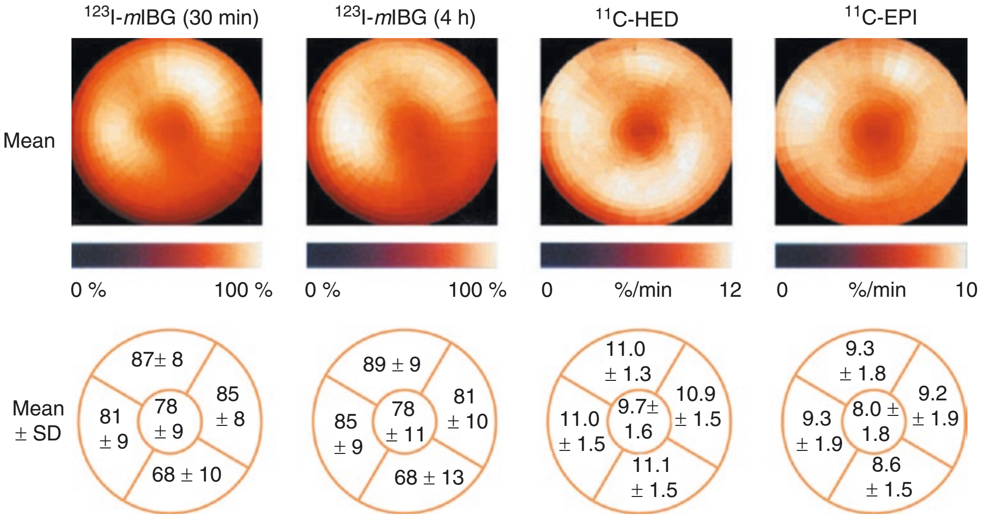

Fig. 11.7 Comparison of a normal tracer distribution of ^{123}I-*m*IBG, ^{11}C-HED, and C-11 epinephrine (^{11}C-EPI) in normal myocardium. For each tracer distribution, 10 patients were imaged following an intravenous injection of 10 mCi ^{123}I-*m*IBG, 20 mCi ^{11}C-HED, and 20 mCi ^{11}C-EPI. The relative tracer distribution normalized to the individual maximum in each patient is displayed in the *lower panel*. Note the slight heterogeneity of tracer retention at 30 minutes and 4 hours after ^{123}I-*m*IBG injection. The relative activity in the inferior segments of the left ventricle, including the apex, shows significantly lower values as compared with the anteroseptal and anterolateral segments. This may represent an attenuation artifact, but inhomogeneous density of the sympathetic nerve terminals in normal myocardium cannot be ruled out. The C-11 tracer retention is expressed as the retention index, which represents tracer activity 40 minutes after tracer injection, normalized to the arterial input function obtained after placing a region of interest over the cavity of the left ventricle [25]. The retention index is expressed as percent per minute (%/min). ^{11}C-EPI retention was obtained 30 minutes after tracer injection and was expressed as the myocardial retention index. These measurements of myocardial PET tracer uptake display greater homogeneity than *m*IBG data. The lower retention index in the apex of the left ventricle most likely represents the partial volume effect during nongated PET data acquisition. PET data are acquired with attenuation correction, but there may be biologic differences in affinity for uptake 1 between *m*IBG and HED

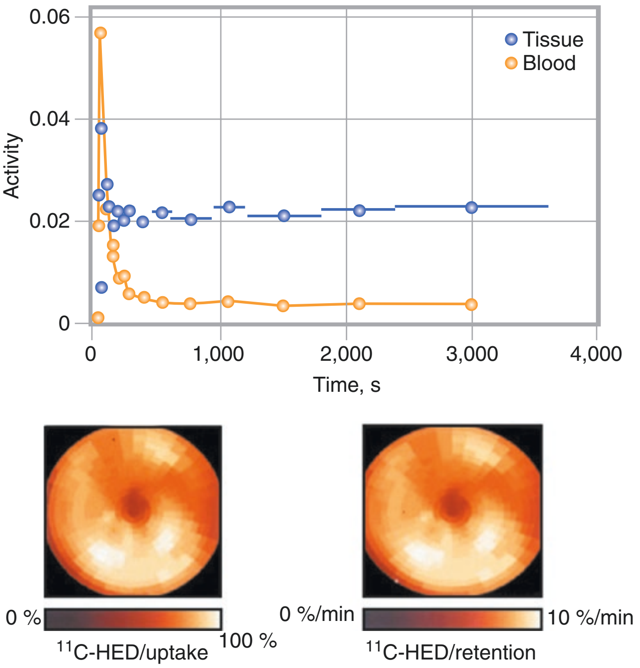

Fig. 11.8 Time–activity curve obtained after the intravenous injection of 20 mCi of ^{11}C-HED in a healthy volunteer. Dynamic PET imaging with a short framing rate allows the determination of tracer time–activity curves of the tissue and blood pool. The time–activity curves were determined using regions of interest placed over the chamber of the left ventricle for the determination of blood activity and placed over the left ventricular myocardium for the tissue activity distribution. The tracer rapidly clears from the blood, resulting in little residual blood activity minutes after the tracer injection. In contrast, the activity obtained from the myocardial region of interest shows stable retention in the myocardium over the time of observation. The initial peak of the myocardial tracer activity measured reflects contamination by blood-pool activity. Dividing this activity measured 30–40 minutes after the tracer injection by the integral of the input function, which reflects the available tracer to the myocardium during this time, yields the calculation of the myocardial retention index. This index averages over 12% in the normal heart

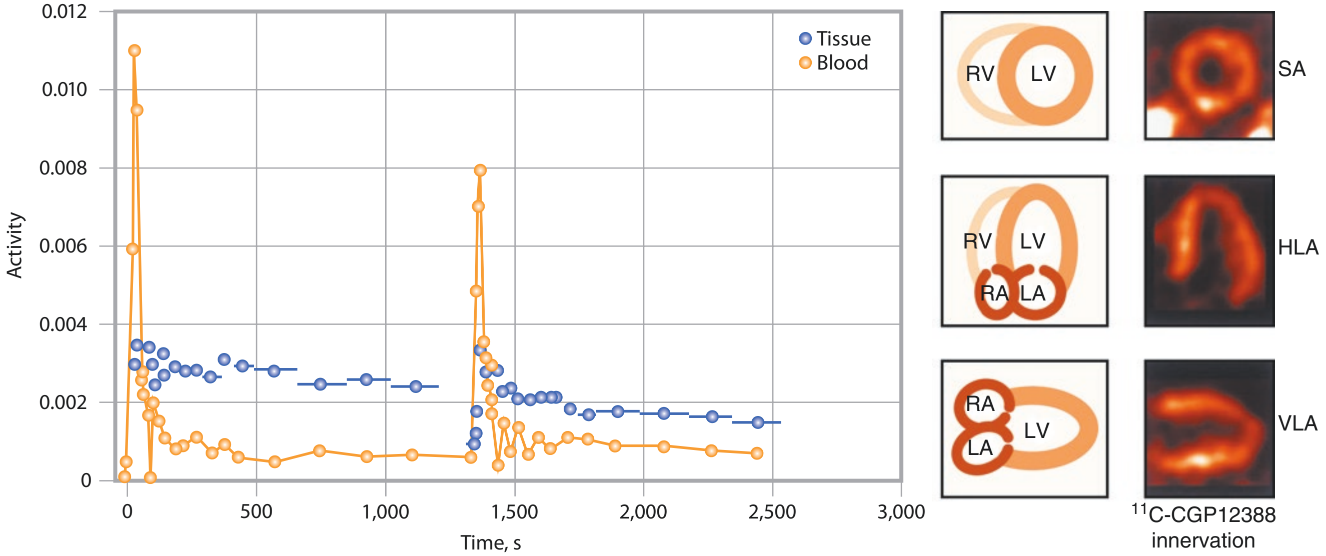

Fig. 11.9 β-Receptor distribution in normal myocardium. PET images following the intravenous injection of β-receptor antagonist ^{11}C-CGP12388 are shown in short-axis (SA), horizontal long-axis (HLA), and vertical long-axis (VLA) images. Images were obtained 40 minutes after the tracer injection and show high contrast between myocardial and nonmyocardial tissue. Pretreatment of patients with cold β-blocker β-receptor antagonists showed reduced tracer retention, suggesting high specific binding to the receptors. However, the shown retention images at 40 minutes primarily represent the delivery of tracer to the myocardium, which is determined by blood flow. To calculate the density of β-receptors in the myocardium, a tracer kinetic model has been proposed by Delforge et al. [27]. A comparison of ^{11}C-CGP measurements with β-receptor density measured in vitro resulted in a linear correlation with high correlation coefficients. Using a tracer kinetic model consisting of two tracer injections with different specific activities, the receptor density can be calculated by curve-fitting procedures of tissue and blood pool–time-activity curves [27]. LA left atrium, LV left ventricle, RA right atrium, RV right ventricle

Heart Failure

PET and SPECT innervation tracers provide valuable information about heart function (Figs. 11.10, 11.11, 11.12, 11.13, 11.14, 11.15, 11.16, 11.17, 11.18, 11.19, and 11.20). Studies have shown that the HMR on ^{123}I-*m*IBG images can distinguish between heart failure (HF) patients at low risk and high risk for mortality (Figs. 11.11, 11.12 and 11.13). PET has quantitative capabilities superior to SPECT, but many useful PET agents are labeled with isotopes that have a short half-life, such as ^{11}C (half-life 20 minutes), which are available only at facilities with on-site cyclotrons. Several ^{11}C-labeled compounds whose uptake is mediated by the NET system have been studied, including HED, epinephrine, and phenylephrine. In addition, ^{18}F-labeled compounds are being developed, including alternative halogenated benzylguanidines with structural similarities to *m*IBG. Studies on normal controls have shown similar myocardial distributions for ^{11}C-HED and epinephrine, as well as for ^{123}I-*m*IBG and the ^{11}C-labeled beta receptor agent CGP12388 [36]. Analogous to studies using ^{123}I-*m*IBG, ^{11}C-HED defects are usually larger than corresponding abnormalities on perfusion imaging. Mismatch between presynaptic neuronal function and postsynaptic beta receptor density has also been demonstrated [41]. Among clinical studies using ^{11}C-HED, PARAPET, a study of 204 patients with ischemic cardiomyopathy, is the largest. In that study, occurrence of arrhythmic death or ICD shock for VT >240 per minute or ventricular fibrillation increased in relation to the severity/extent of ^{11}C-HED defects (hazard ratio per 1% of LV 1.069 in multivariate analysis; $p = 0.003$); neither infarct volume nor hibernating myocardium were significant predictors as continuous variables [42]. Other small studies have suggested that absolute ^{11}C-HED quantification is possible using venous blood samples [43] and that dynamic PET data can be used to estimate both blood flow and neuronal uptake, thereby eliminating the need for a separate perfusion study [44].

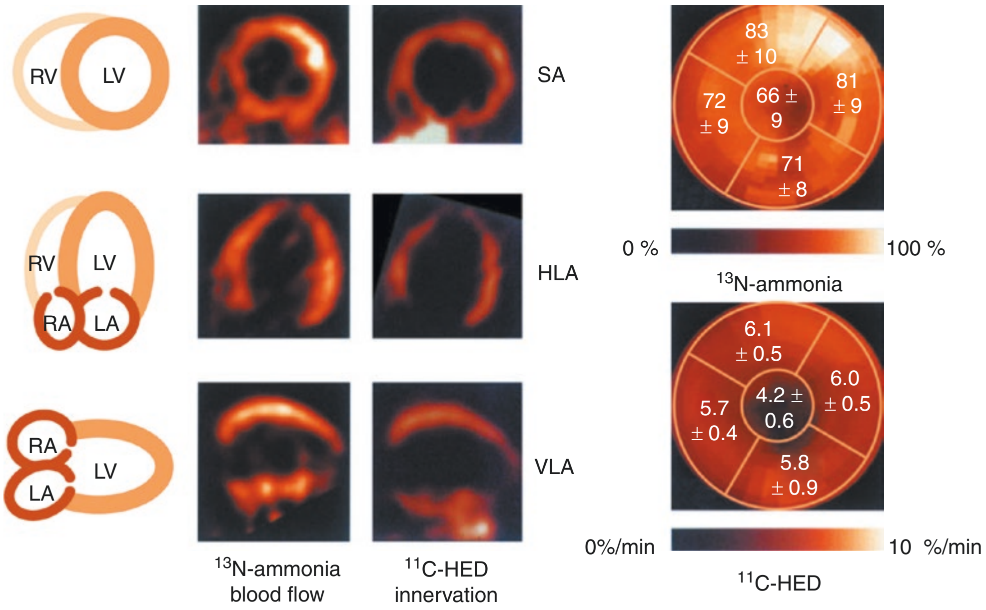

Fig. 11.10 Increased activity of the sympathetic nervous system: a hallmark of heart failure. Plasma levels of norepinephrine are elevated, myocardial norepinephrine reuptake is reduced, and myocardial β-receptors are downregulated, reflecting generalized adrenergic activation [2, 3]. Enhanced sympathetic activity increases myocardial contractility and heart rate and (via increased preload) activates the Frank–Starling mechanism. These responses are capable of maintaining ventricular performance and cardiac output for a limited time, but adrenergic activation eventually contributes to deterioration of cardiac function and the progression of heart failure. In comparison to healthy subjects, retentions of ^{11}C-HED and ^{123}I-*m*IBG are abnormally reduced in heart failure patients [20, 28, 29]. In this example, a patient with dilated cardiomyopathy and reduced left ventricular function was imaged with PET following the injection of ^{13}N-ammonia and 40 minutes after the injection of ^{11}C-HED. The tomographic slices are displayed in short-axis (SA), horizontal long-axis (HLA), and vertical long-axis (VLA) views. There is relatively homogeneous distribution of ^{13}N-ammonia, indicating the integrity of myocardial perfusion, but the retention of ^{11}C-HED is markedly reduced, indicating partial denervation of the left ventricle (LV). The quantitative retention index of ^{11}C-HED is reduced to 6% (normal >12%). The area of denervation is most evident in the distal anterior wall and apical area of the LV, which is consistent with the injury of the autonomic nervous system being a heterogeneous process in patients with congestive heart failure [28]. Furthermore, a mismatch between presynaptic and postsynaptic sympathetic function with a more pronounced reduction of ^{11}C-HED retention compared with β-adrenergic receptor density as assessed by β-receptor antagonist ^{11}C-CGP12177 is common in patients with ischemic heart failure [29]. LA left atrium, RA right atrium, RV right ventricle

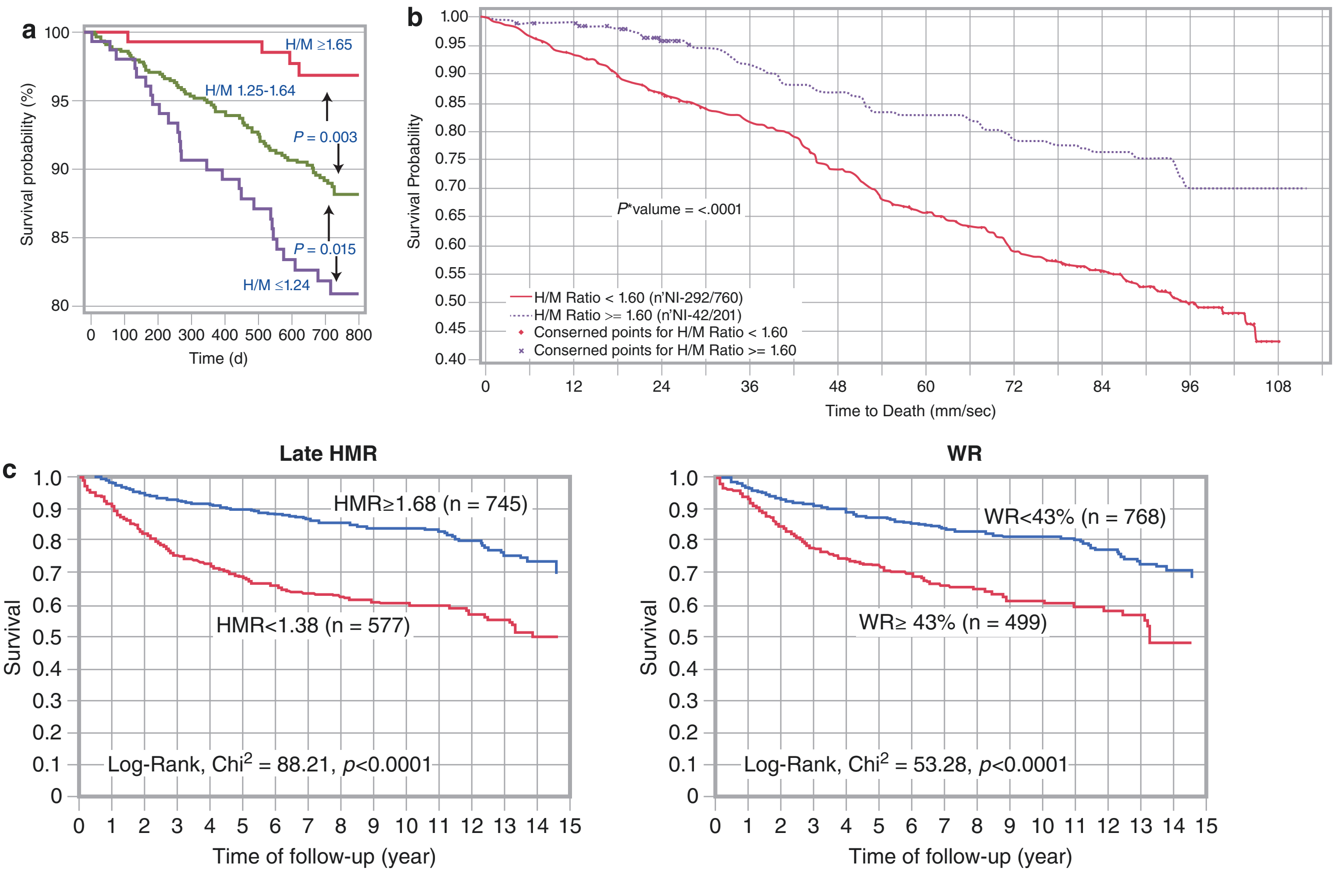

Number at risk

Year	0	1	2	3	5	7	10
🟦 HMR≥1.68	745	729	689	634	438	288	179
🟥 HMR<1.68	577	526	466	403	290	190	123

Number at risk

Year	0	1	2	3	5	7	10
🟦 WR<43%	768	746	700	643	450	330	228
🟥 WR≥43%	499	465	415	359	257	129	60

Fig. 11.11 The planar HMR has demonstrated excellent discriminative power for distinguishing between heart failure (HF) patients at low risk and high risk for cardiac and all-cause mortality. In the prospective ADMIRE-HF study of 961 NYHA class II and III HF patients, the prespecified HMR ≥1.60 identified a population with <2% annual mortality to 2 years. (**a**) Further survival analyses on the basis of the population mean HMR (1.44) ± SD (0.20) provided distinct separation of subjects into low-risk, intermediate-risk, and high-risk groups: Two-year mortality was 3.1% for HMR ≥1.65 (n = 147), 11.8% for HMR 1.25–1.64 (n = 660), and 19.1% for HMR <1.25 (n = 154) [30]. (**b**) The low-risk population (HMR ≥1.60) had persistence of the survival benefit on longer follow-up, with 5-year all-cause mortality rate of 25.8% versus 49.1% for HMR <1.60 (p < 0.0001) [31]. (**c**) In a prospective meta-analysis of 1322 HF patients in Japan who underwent ^{123}I-*m*IBG imaging and were followed for up to 15 years, there was significantly better survival in patients with preserved myocardial sympathetic innervation, as reflected by the threshold values of late HMR ≥1.68 and washout rate (WR) <43%. (From Nakata et al. [32]; with permission from Elsevier)

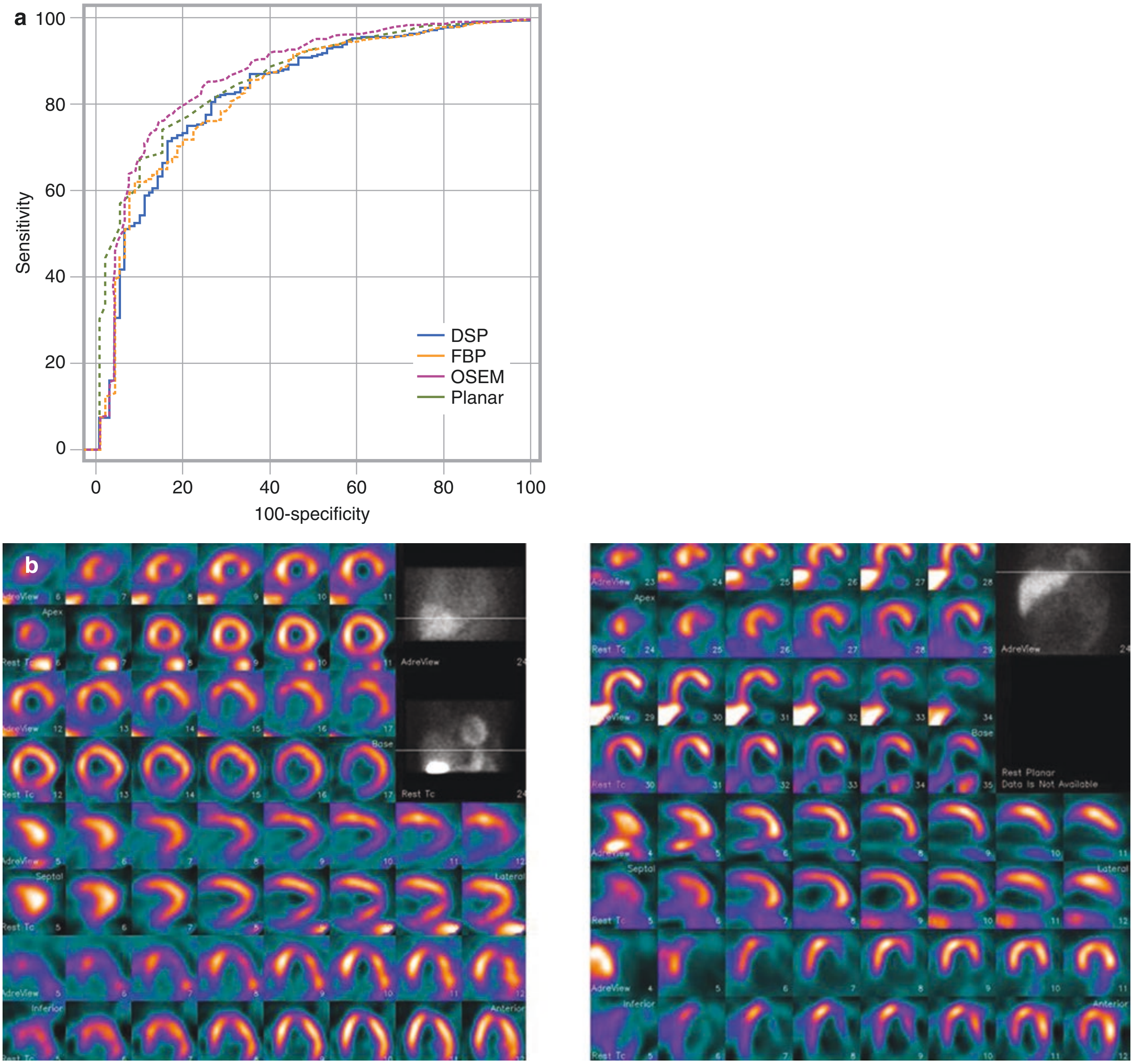

mIBG Defect Score = 14;
Innervation/perfusion mismatch

mIBG Defect Score = 22;
Innervation/perfusion match

Fig. 11.12 ^{123}I-*m*IBG SPECT can provide both global quantitation with discrimination similar to planar imaging and regional data not available on planar views. Comparisons between planar HMR determinations and measurements derived from conventional Anger camera SPECT have shown good correlation and similar capability for discriminating between normal and abnormal innervation. (**a**) ROC curve comparison of HMR discrimination between control subjects without heart disease (n = 90) and subjects with HF (n = 926). Among over 1000 patients studied with both planar and conventional ^{123}I-*m*IBG SPECT, although SPECT HMRs were consistently higher than planar, there was no difference in discrimination capability between the 90 controls and 926 HF patients using ROC curves [33]. Three SPECT reconstruction techniques were used: deconvolution of septal penetration (DSP), filtered back projection (FBP), and ordered subset expectation-maximization (OSEM). There were no significant differences among the areas under the curve (AUC) for the planar and three SPECT determinations. (From Chen et al. [33], with permission from Springer Nature.) (**b**) ^{123}I-*m*IBG and myocardial perfusion imaging (MPI) SPECT are often compared to identify perfused but denervated myocardium. Multiple studies have shown ^{123}I-*m*IBG SPECT defect severity to be predictive of adverse outcomes such as cardiac death and arrhythmic events, but innervation/perfusion mismatch severity has been less consistently predictive. SPECT studies pictured [^{123}I-*m*IBG (rows 1, 3, 5, and 7) and rest ^{99m}Tc-tetrofosmin (rows 2, 4, 6, and 8)] are from two patients with ischemic HF. MIBG defect scores are based on visual assessment using a standard 17-segment model (score 0–4, maximum 68). Patient on the left has moderate cavity dilatation on MPI, but uptake is nearly normal except for a small area at the base of the inferior septum. There is a larger abnormality in the inferior wall on the ^{123}I-*m*IBG images, representing an area of innervation/perfusion mismatch (^{123}I-*m*IBG defect score, 14). Patient on the right has a large matched defect in the inferior and inferolateral walls on both ^{123}I-*m*IBG and tetrofosmin images (^{123}I-*m*IBG defect score, 22).

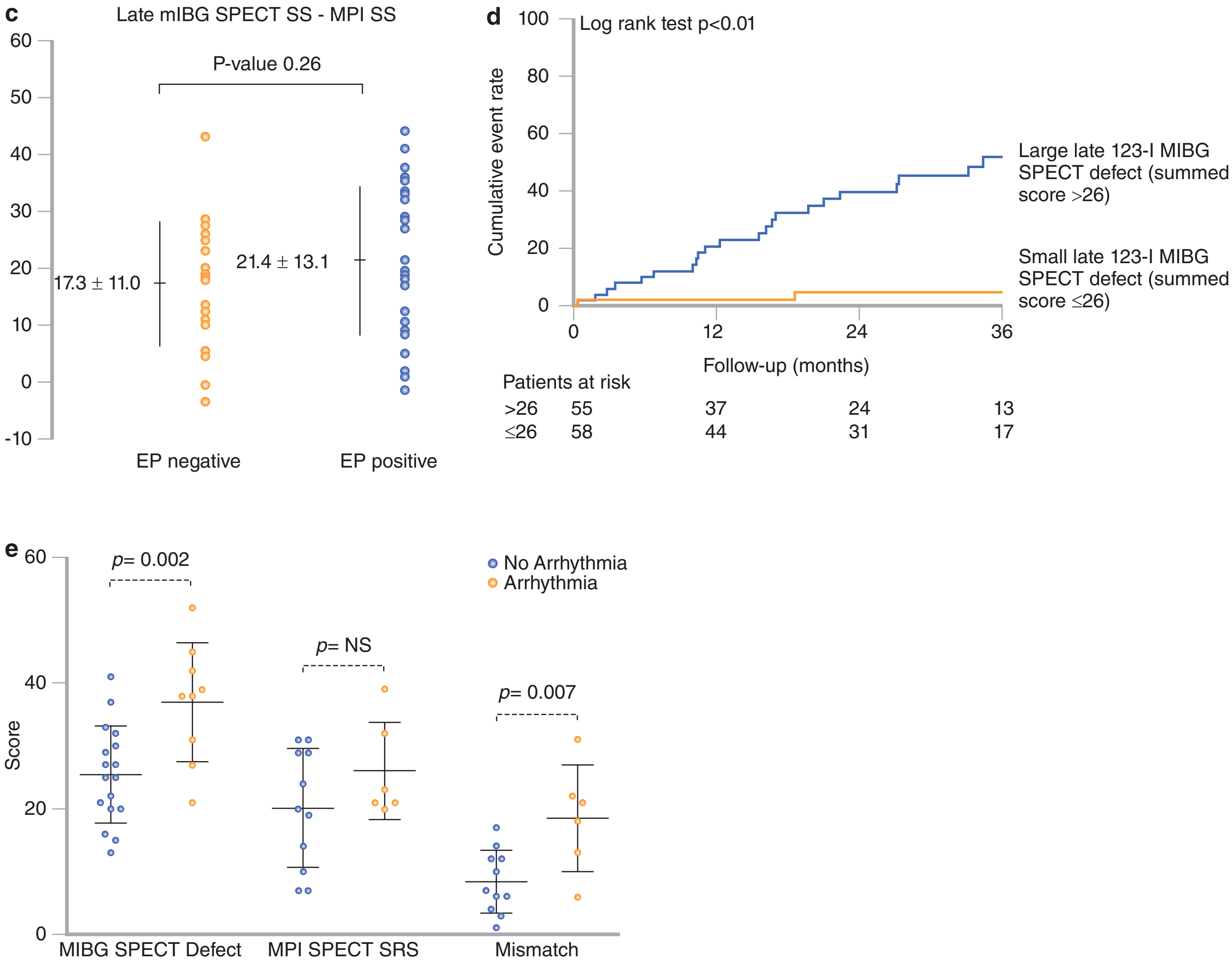

Fig. 11.12 (continued) (**c**–**e**) Discordant analyses examining the prognostic significance of mismatch between *m*IBG and MPI SPECT for the occurrence of arrhythmic events. (**c**) In a study of 50 ischemic heart disease patients referred for electrophysiology (EP) testing, the mismatch score was not predictive of inducibility of sustained VT (A) [34]. (**d**) However, a study of 116 HF patients referred for ICD implantation (B) found the ^{123}I *m*IBG/perfusion mismatch score predictive of subsequent ICD shock on univariate Cox analysis (HR = 1.06 [1.02–1.09], $p < 0.01$) but not on multivariate Cox analysis (HR = 1.01 [0.97–1.06], $p = 0.5$) [35]. (**e**) A small study of 27 HF patients referred for ICDs (C) did show significance of the mismatch score as a predictor of ICD activations during a mean follow-up of 16 months [36]. In all three studies, the *m*IBG SPECT defect score was a significant predictor of subsequent arrhythmic events. In aggregate, these and other studies have confirmed that medium to large innervation defects on *m*IBG SPECT studies (typically involving 20–50% of the myocardium) are associated with increased risk for arrhythmias

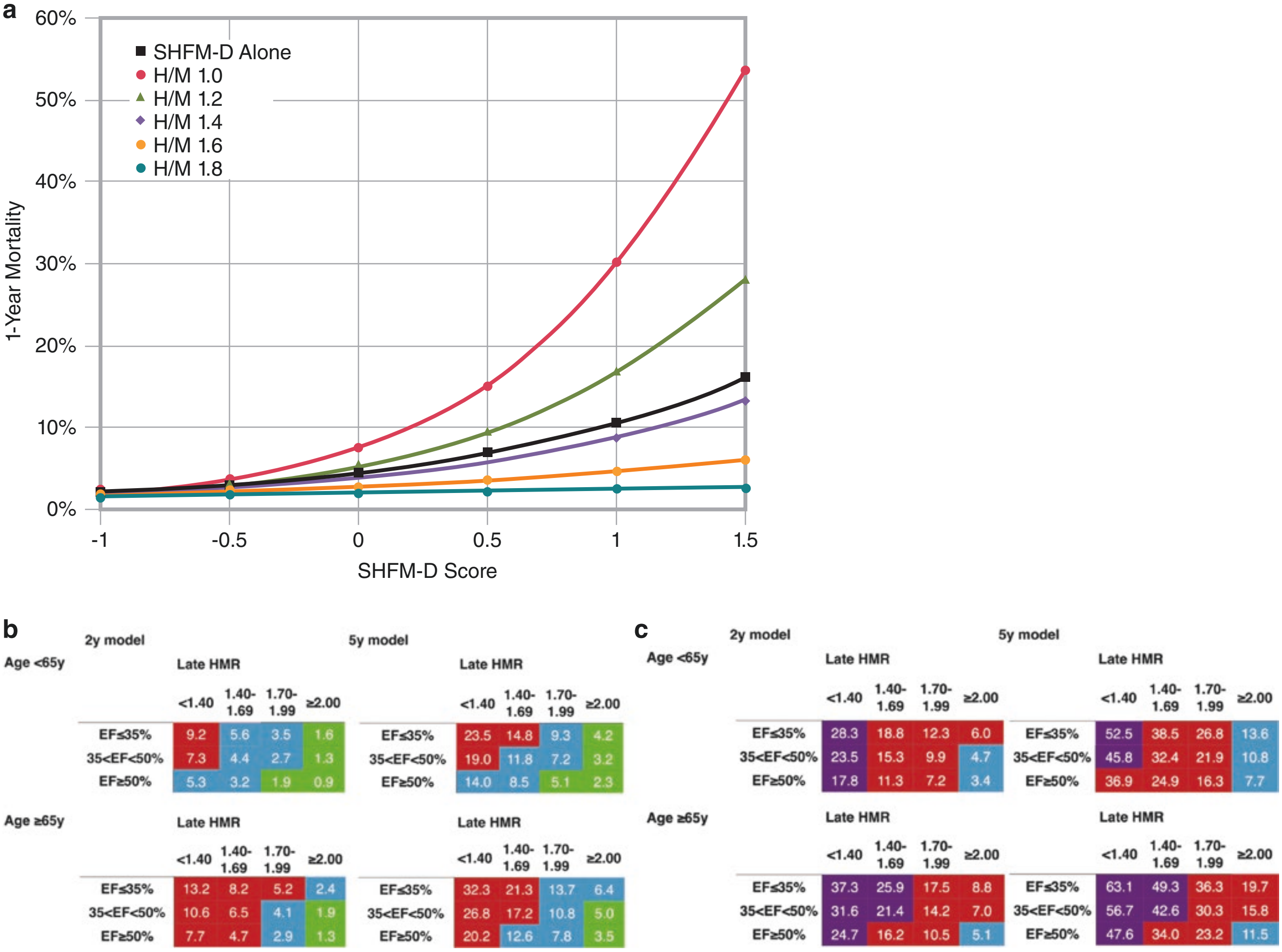

b

2y model, Age <65y

Late HMR	<1.40	1.40-1.69	1.70-1.99	≥2.00
EF≤35%	9.2	5.6	3.5	1.6
35<EF<50%	7.3	4.4	2.7	1.3
EF≥50%	5.3	3.2	1.9	0.9

5y model, Age <65y

Late HMR	<1.40	1.40-1.69	1.70-1.99	≥2.00
EF≤35%	23.5	14.8	9.3	4.2
35<EF<50%	19.0	11.8	7.2	3.2
EF≥50%	14.0	8.5	5.1	2.3

2y model, Age ≥65y

Late HMR	<1.40	1.40-1.69	1.70-1.99	≥2.00
EF≤35%	13.2	8.2	5.2	2.4
35<EF<50%	10.6	6.5	4.1	1.9
EF≥50%	7.7	4.7	2.9	1.3

5y model, Age ≥65y

Late HMR	<1.40	1.40-1.69	1.70-1.99	≥2.00
EF≤35%	32.3	21.3	13.7	6.4
35<EF<50%	26.8	17.2	10.8	5.0
EF≥50%	20.2	12.6	7.8	3.5

c

2y model, Age <65y

Late HMR	<1.40	1.40-1.69	1.70-1.99	≥2.00
EF≤35%	28.3	18.8	12.3	6.0
35<EF<50%	23.5	15.3	9.9	4.7
EF≥50%	17.8	11.3	7.2	3.4

5y model, Age <65y

Late HMR	<1.40	1.40-1.69	1.70-1.99	≥2.00
EF≤35%	52.5	38.5	26.8	13.6
35<EF<50%	45.8	32.4	21.9	10.8
EF≥50%	36.9	24.9	16.3	7.7

2y model, Age ≥65y

Late HMR	<1.40	1.40-1.69	1.70-1.99	≥2.00
EF≤35%	37.3	25.9	17.5	8.8
35<EF<50%	31.6	21.4	14.2	7.0
EF≥50%	24.7	16.2	10.5	5.1

5y model, Age ≥65y

Late HMR	<1.40	1.40-1.69	1.70-1.99	≥2.00
EF≤35%	63.1	49.3	36.3	19.7
35<EF<50%	56.7	42.6	30.3	15.8
EF≥50%	47.6	34.0	23.2	11.5

Fig. 11.13 Prediction models including *m*IBG results. There are numerous multivariate models for predicting the likelihood of adverse cardiovascular outcomes and death. *m*IBG results have been examined in conjunction with such models and have consistently proven to have independent predictive value. (**a**) The Seattle HF Model (SHFM) has been widely validated as a predictor of mortality in HF patients. The graph demonstrates the effect of adding *m*IBG imaging results to this multivariate clinical risk model for predicting 1-year all-cause mortality. Mortality estimates for the ADMIRE-HF population using SHFM version D (SHFM-D) [33] are represented by the black line with squares. Addition of the planar H/M ratio at five different levels (1.0, 1.2, 1.4, 1.6, and 1.8) is represented by the other lines in the graph [37]. Whereas an H/M ratio of 1.4 produces little change in the risk estimate, as the H/M value decreases, risk rises substantially. For an SHFM-D score of 1, equivalent to a 1-year mortality rate of about 10%, an HF patient with an H/M of 1.0 has a predicted mortality rate three times higher. Conversely, an H/M of 1.8 is associated with a greater than three times reduction in risk. Analyses of the same source data using risk models developed from four large prospective trials (EFFECT, Care-HF, MADIT-II, and PACE) produced similar results, with the addition of H/M ratio to each model providing improved HF risk assessment [38]. (From Jain et al. [38], with permission.) (**b**–**d**) Risk models were created based upon a Japanese meta-analysis population of 1322 HF patients followed for up to 15 years [39]. Practical utility dictated creation of two models, one for 2-year outcomes and one for 5-year outcomes. To provide a complete data set for 2-year analysis, 1280 patients who had definitive 2-year outcomes (death or survival) were included. Similarly, 933 patients who had complete information on 5-year outcomes were included for the 5-year analysis. The two-year logistic regression model included NYHA class, late HMR, and age as significant variables; the left ventricular ejection fraction (LVEF) was of borderline significance ($p = 0.054$). In the 5-year group, NYHA class, late HMR, age, and LVEF were significant variables. Cardiac mortality risk charts were then created using suitable aggregations of the four relevant variables. *Chart A* is for NYHA class I and II, while *Chart B* is for NYHA class III and IV. Color coding clearly shows the progressive increase in mortality risk with decreasing HMR: green <1%; blue 1.0–2.9%; red 3–9.9%; purple ≥10%. (**d**) Survival curves from a validation population of different HF patients (n = 546), in whom the 2-year cardiac death model was accurate for identifying low risk (<4%), and intermediate risk (4–12%), with actual 2-year cardiac mortality of 1.1% and 7.9% respectively. The model underestimated cardiac mortality for high-risk patients, presumably because the validation population had more severe HF than the derivation population [40]. (**a** and **b** from Nakajima et al. [39] and **c** from Nakajima et al. [40], with permission from Oxford University Press)

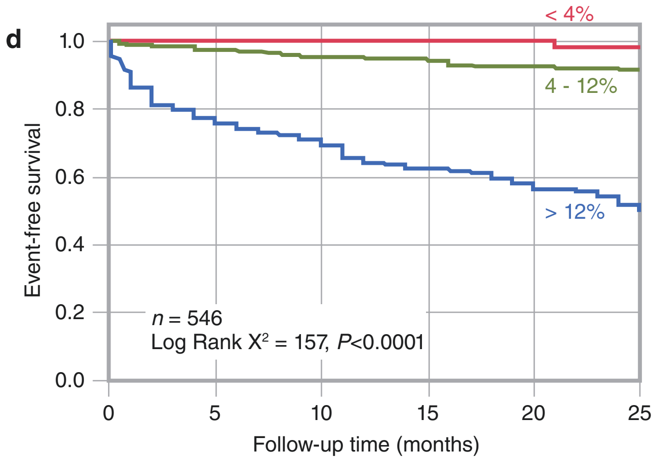

Number at risk	0 month	24 months
<4%	85	60
4-12%	291	188
>12%	170	65

Fig. 11.13 (continued)

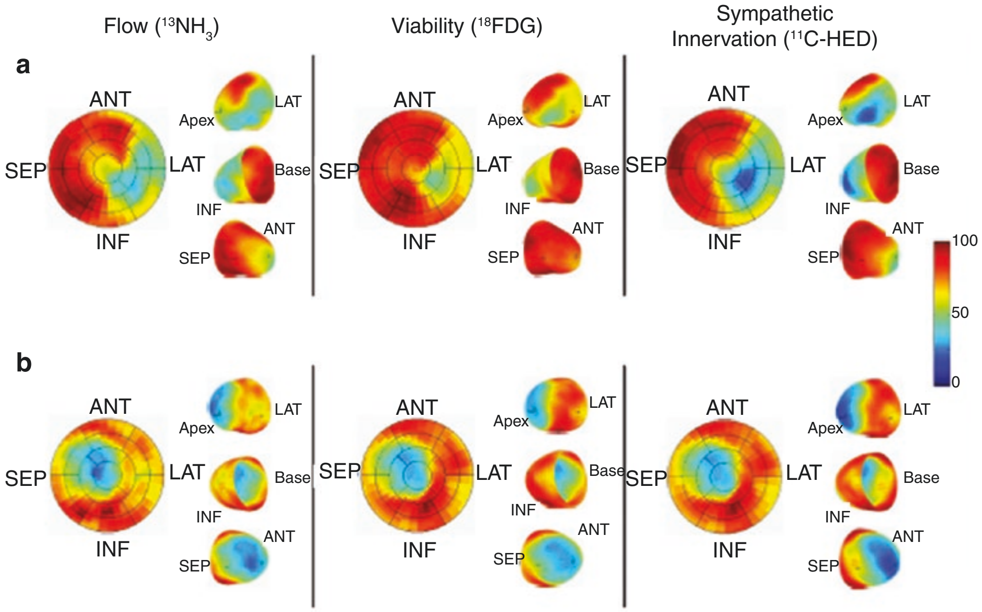

Fig. 11.14 Quantitative displays from PET imaging of myocardial blood flow ($^{13}NH_3$), viability (^{18}F-FDG), and sympathetic innervation (^{11}C-HED). Subject A, who experienced sudden cardiac arrest, had a larger innervation defect than the area of infarct shown by FDG. Subject B had a matched defect on flow, viability, and innervation imaging. (From Fallavollita et al. [42], with permission from Elsevier)

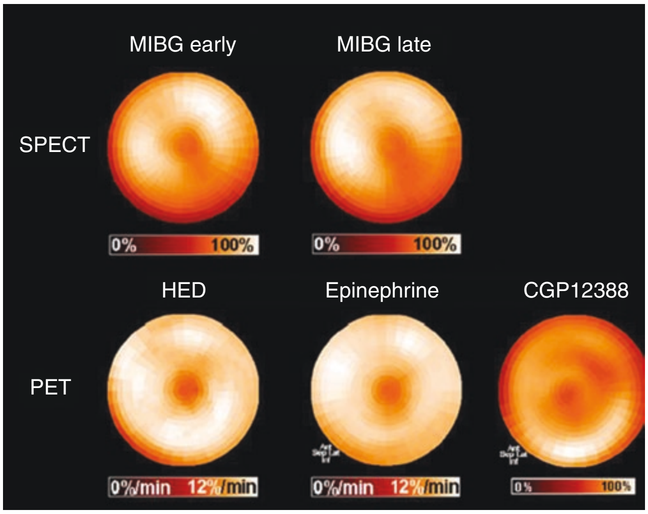

Fig. 11.15 Polar maps of myocardial distribution (center–apex to periphery–base) of *m*IBG from early (15 minutes post-injection) and late (4 hours post-injection) SPECT images of the normal heart for comparison with those of selected ^{11}C-labeled PET tracers also used in assessment of functional status of the sympathetic nervous system. The mechanism of neuronal uptake for HED and epinephrine are the same as for *m*IBG, with the norepinephrine transporter (NET) responsible for transfer of the compounds into the neuronal cytoplasm. ^{11}C-labeled CGP12388 binds to post-synaptic beta receptors, providing a means to assess the distribution and density of these adrenergic receptors. Distribution patterns for all five image sets are equivalently uniform, confirming that all tracers are interrogating attributes of the same physiological system. (From Bengel et al. [45], with permission from Springer Nature)

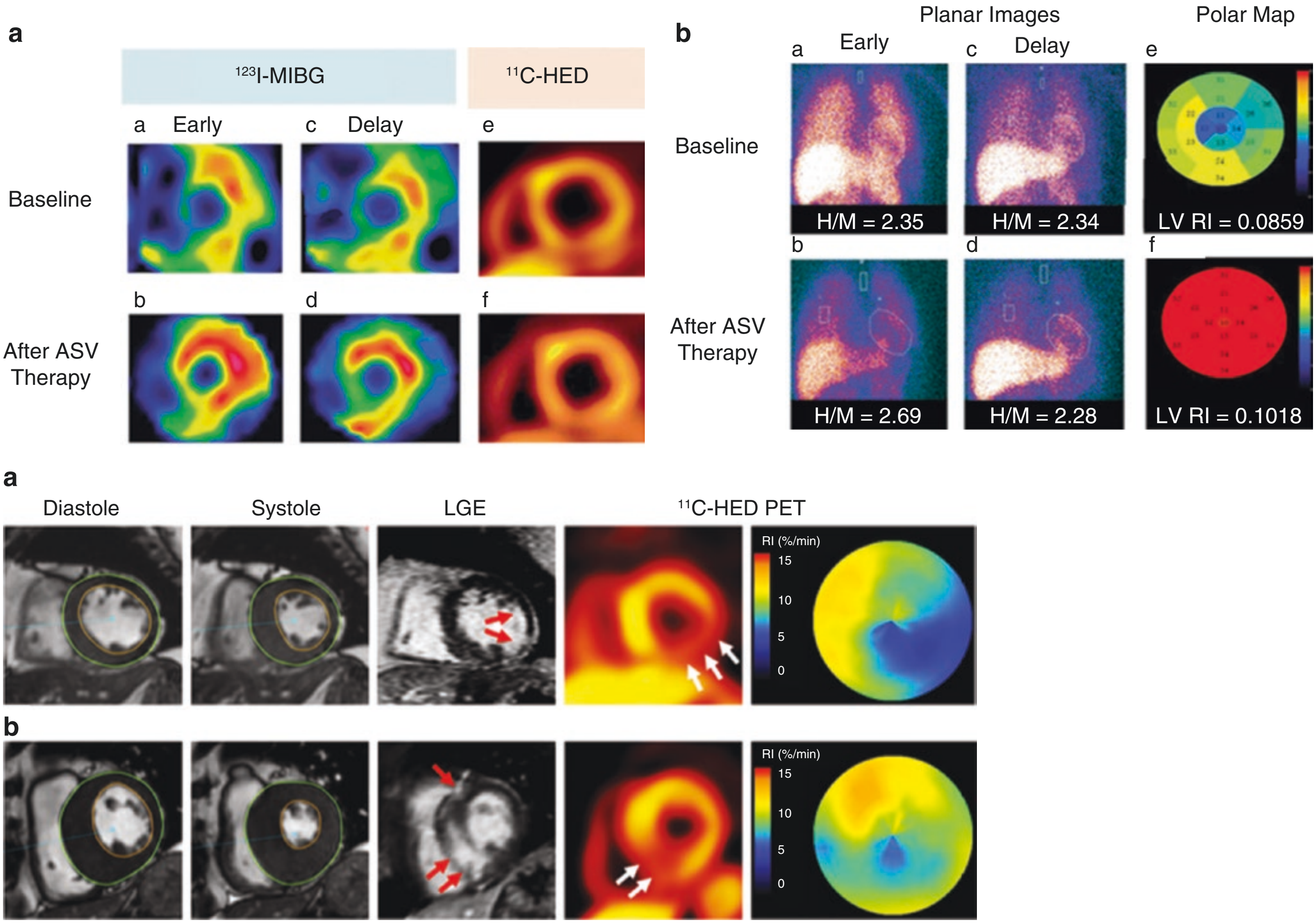

Fig. 11.16 The short half-life of ^{11}C and somewhat more rapid neuronal turnover of HED compared with *m*IBG requires use of a different quantitative technique for ^{11}C-HED. The most commonly used parameter for ^{11}C-HED is the retention index (RI), typically calculated by dividing mean global or segmental activity from a late image (between 15 and 60 minutes post-injection) by the integrated arterial activity during the entire dynamic acquisition. Comparisons can be performed with the myocardial segment with the highest RI or with data from control subjects without heart disease [46]. There is a growing body of evidence that ^{11}C-HED imaging results have diagnostic and prognostic significance comparable to those from *m*IBG imaging. In a study of early therapeutic effects of adaptive servoventilation (ASV) in HF patients studied with both *m*IBG and ^{11}C-HED, there was improvement from baseline in both early HMR and RI at 6 months after initiation of the therapy [47]. (**a**) In this example from a 27-year-old woman with HF whose LVEF increased from 38.0% to 45.0% after ASV therapy (A and B), global neuronal function improved on both *m*IBG (early HMR increasing from 2.35 to 2.69) and ^{11}C-HED (RI increasing from 0.086 to 0.102). (From Tokuda et al. [47], with permission from Springer Nature.) (**b**) Another ^{11}C-HED PET study involved 34 patients with HF with preserved ejection fraction (HFpEF) and 11 control subjects who also underwent cardiac MRI with late gadolinium enhancement (LGE) to measure left ventricular size, function, and myocardial infarct extent [48]. In the examples in Panel B1, row *a* is from a 65-year-old man with prior lateral myocardial infarction. There is lateral wall LGE consistent with subendocardial infarction (*red arrows*) and reduced ^{11}C-HED uptake (*white arrows*), which exceeds the extent of LGE. The polar map of the ^{11}C-HED RI shows a regional decrease in the inferior to lateral wall. In row *b*, from a 65-year-old man with hypertrophic cardiomyopathy, the LGE image shows hyperenhancement in the interventricular septum at the insertion points of the right ventricle (*red arrows*) and the ^{11}C-HED PET image and the polar map show regional decrease in the septal to inferior wall (*white arrows*). (**c**) Graphs shows aggregate study results. In part a, there is modest stepwise decrease in regional ^{11}C-HED RI with increasing LGE extent and decreasing wall thickening (WT). In part b, impaired regional RI (<10%/min; the lower quartile value of the control group segments) was found in 76% of all segments in 32 patients with HFpEF (excluding two patients with cardiac amyloidosis). (**d**) The majority of segments with impaired regional ^{11}C-HED RI had decreased systolic wall thickening and the presence of LGE. Numbers in parentheses are numbers of segments. (From Aikawa et al. [48]; CC-BY)

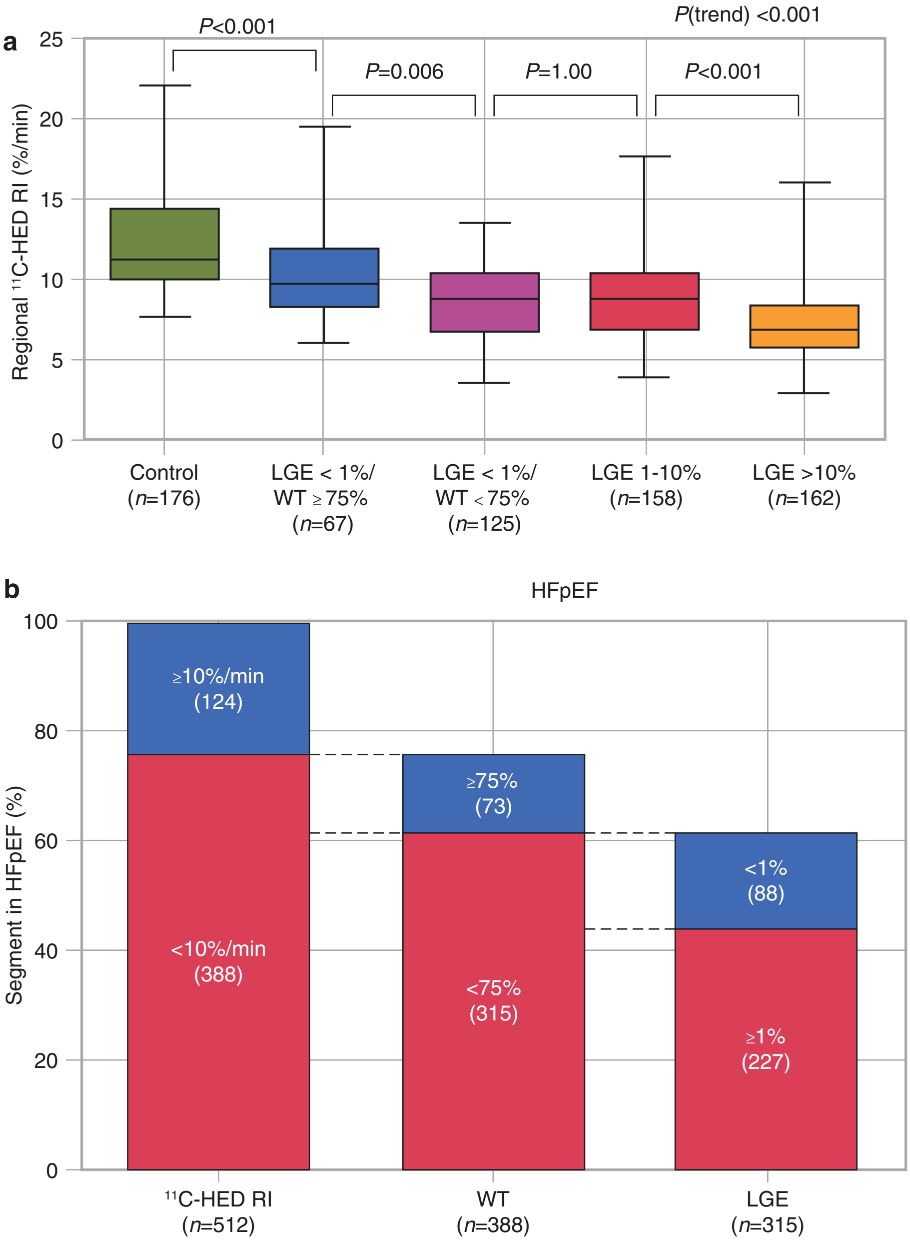

Fig. 11.16 (continued)

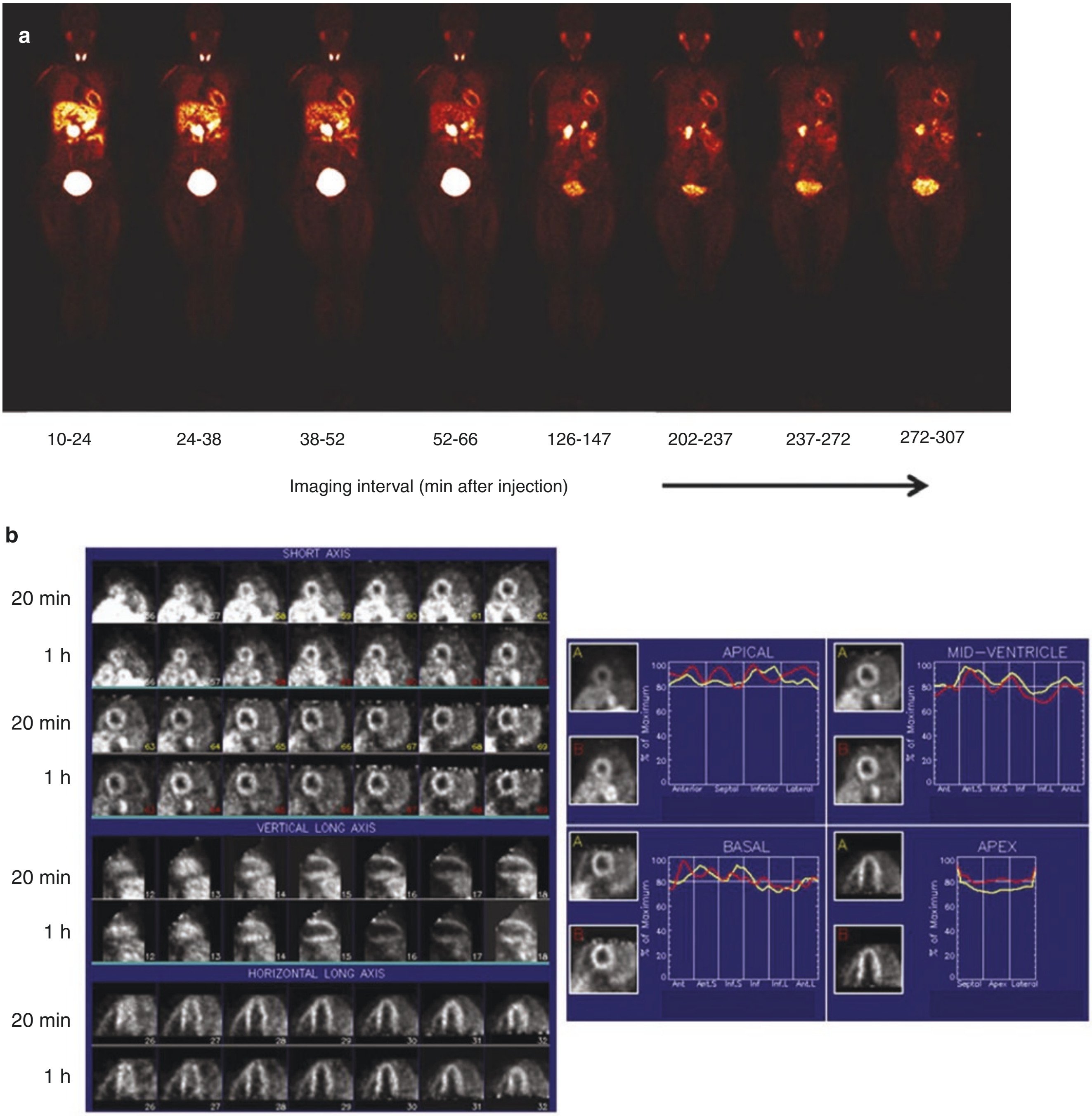

Fig. 11.17 LMI1195 is one of several ^{18}F-labeled benzylguanidines under development [49]. (**a**) Sequence of whole-body LMI1195 coronal images at mid-myocardial level in a human volunteer. Cardiac uptake is evident at 10–24 minutes after injection and remains clearly seen up to 5 hours. (**b**) Reoriented short-axis, vertical long-axis, and horizontal long-axis LMI1195 cardiac images in a healthy volunteer at 20 minutes and 1 hour after radiotracer injection (*left*) and circumferential quantitative profiles obtained in the same patient (*right*) [49]

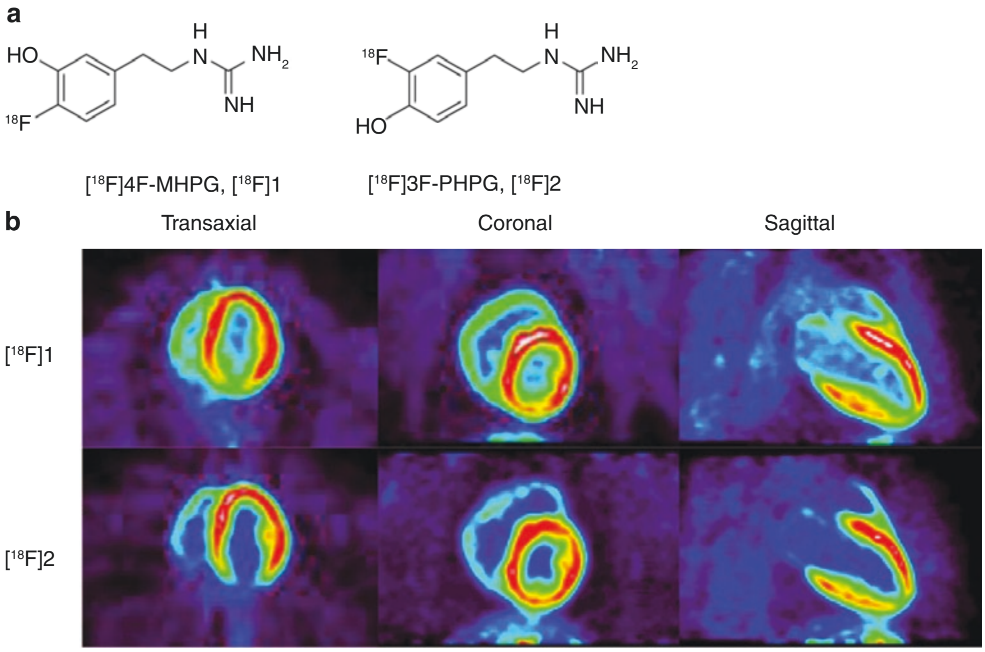

Fig. 11.18 A promising group of compounds for studying cardiac sympathetic innervation is the [^{18}F]Fluoro-Hydroxyphenethylguanidines. Preliminary animal studies have presented encouraging results, as has early human imaging [50]. (**a**) The structural formulas for two candidate molecules. (**b**) Cardiac images in rhesus macaque monkeys. (From Jung et al. [50]; with permission from the American Chemical Society)

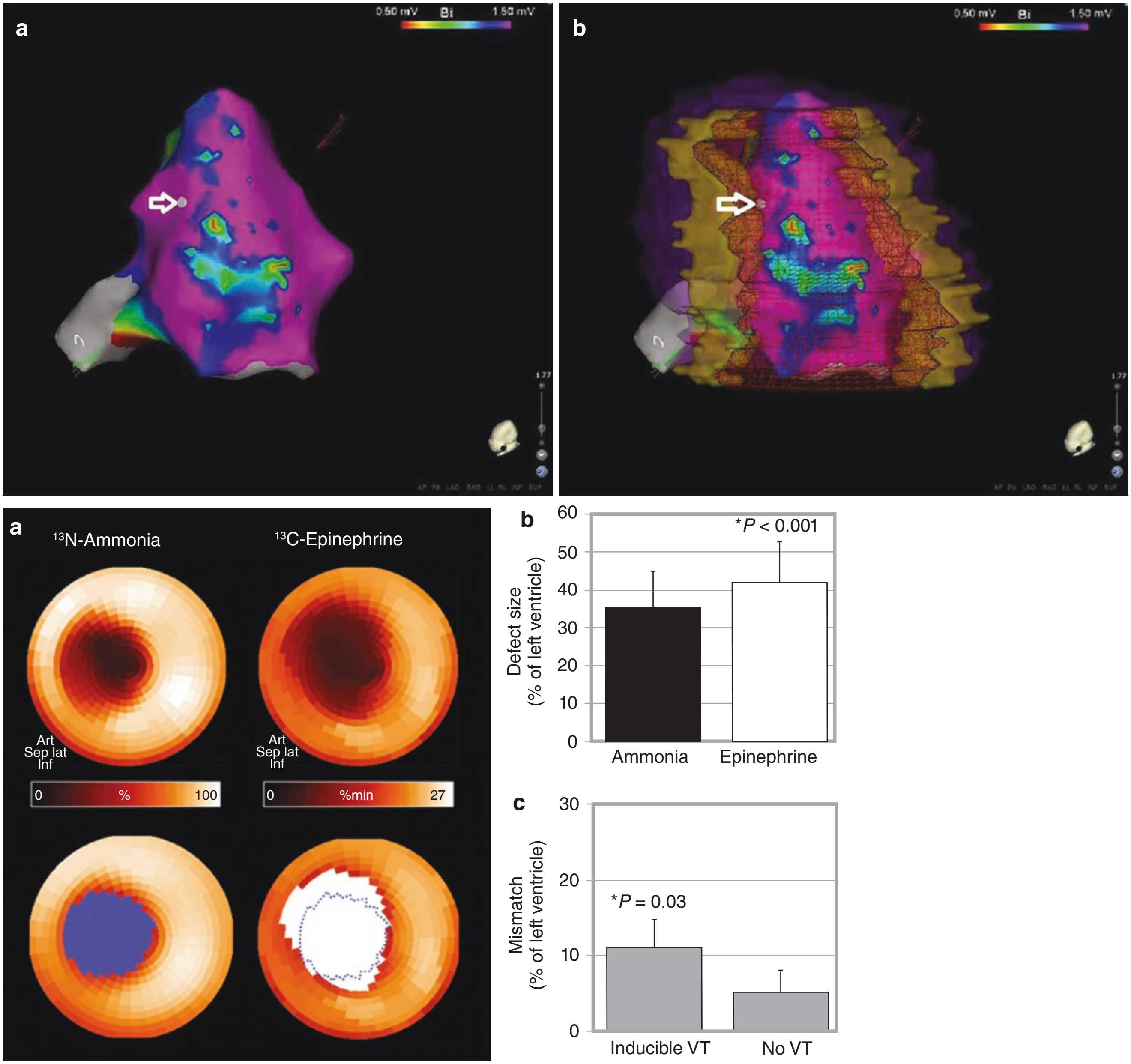

Fig. 11.19 PET and SPECT innervation tracers have been used to study the border zone surrounding myocardial infarct, a region believed to be arrhythmogenic. In a quantitative analysis of ^{123}I-*m*IBG SPECT images from coronary artery disease patients who underwent electrophysiology testing, the best predictor of VT inducibility was ^{123}I-*m*IBG uptake in the border zone (area under ROC = 0.78)—better than MPI scar extent or border zone extent [51]. In a prospective study of 15 patients referred for ischemic VT ablation and studied with ^{123}I-*m*IBG SPECT and high-density voltage mapping [52], ^{123}I-*m*IBG innervation defects were about 2.5-fold larger than bipolar voltage-defined scars, all VT ablation sites were within areas of abnormal innervation, and 36% of successful ablation sites demonstrated normal voltages (>1.5 mV). (**a**) In this example of a discordant preserved voltage-denervation location of a successful ablation site, the bipolar electroanatomic map, inferior view (A), demonstrates inferior scar with ablation site (*yellow dot*; *white arrow*) at an inferior septal location within the area of preserved bipolar voltage (>1.5 mV). Coregistration of the electroanatomic bipolar voltage map and innervation map (B) demonstrates a significantly larger area of denervation than bipolar voltage scar or border zone. The successful ablation point (*yellow dot*; *white arrow*) is located within the area of denervation close to the denervation/neuronal transition zone interface despite preserved bipolar voltage (^{123}I-metaiodobenzylguanidine transition zone in overlying transparent yellow, and normally innervated myocardium in overlying transparent purple) [52]. (**b**) Perfusion/innervation mismatch has been studied in an animal model of MI [53]. Panel A shows representative PET polar maps of myocardial perfusion (^{13}N-ammonia) and innervation (^{11}C-epinephrine). The innervation defect (*white area*) is larger than the perfusion defect (*blue area*), resulting in an area of normally perfused myocardium with impaired innervation in the infarct border zone. Panel B shows defect sizes in all animals (n = 13). Panel C compares the perfusion/innervation mismatch in subgroups with (n = 5) and without (n = 6) inducible VT. As expected, inducibility was associated with larger areas of mismatch [53]

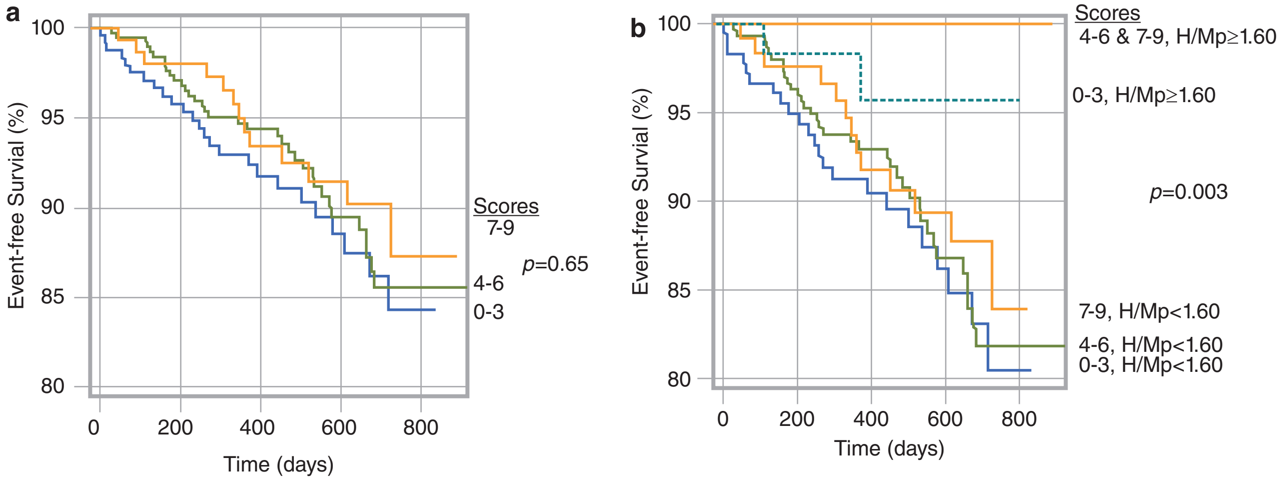

Fig. 11.20 (**a**) Survival curves from the ADMIRE-HF study categorized in terms of baseline HF medication intensity (0–9 score based on doses of beta blockers, ACE inhibitors, angiotensin receptor blockers, and aldosterone antagonists) (Panel A) and medication score and planar HMR (HMR_p) subcategorized as normal ($HMR_p \geq 1.60$) or abnormal ($HMR_p < 1.60$) (Panel B). There is no difference in 2-year survival based on the medication categories alone, but significantly better survival for patients with $HMR_p \geq 1.60$ in all medication score subgroups. This demonstrates that point-in-time assessment of cardiac sympathetic innervation status has independent prognostic value regardless of the current treatment regimen. (From Pina et al. [54], with permission.) (**b**) In an analysis of medications used by ADMIRE-HF subjects, the 71 subjects who had taken higher-potency (with respect to NET inhibition) antidepressants (tricyclic antidepressants and SNRIs) had lower HMRs than the 78 who took other neuropsychiatric medications (1.400 ± 0.189 *vs*. 1.476 ± 0.192, $p = 0.017$) [55]. Nevertheless, the predictive capability of the dichotomous HMR threshold of 1.60 was maintained, even among those taking the higher-potency inhibitors. Overall, there were no deaths to 2 years among the 13 HF patients taking the higher-potency medications who had an HMR ≥1.60, compared with 5 deaths (9%) among the higher-potency group with HMR <1.60. (From Jacobson et al. [55]; with permission from Wolters Kluwer)

Ischemic Heart Disease

Figures 11.21 and 11.22 illustrate imaging performed following myocardial infarction, suggesting that sympathetic neurons are more sensitive to ischemia than myocytes, and that denervated but viable myocardium can then form a substrate for ventricular arrhythmias.

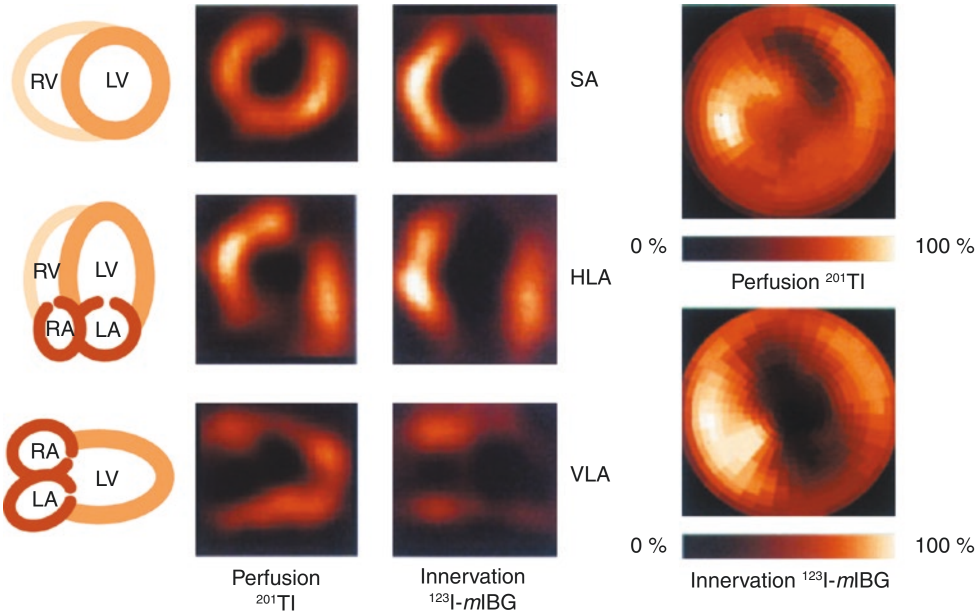

Fig. 11.21 Sympathetic nerve terminals are susceptible to ischemic damage, as illustrated in these SPECT images that were obtained in a patient within 14 days of an anterior myocardial infarction [56–58]. The tomographic slices are displayed in short-axis (*SA*), horizontal long-axis (*HLA*), and vertical long-axis (*VLA*) views. Regional retention of ^{123}I-*m*IBG 4 hours after administration of 10 mCi was compared with the myocardial perfusion as assessed from images acquired 20 minutes after an injection of 2 mCi of thallium-201 (^{201}Tl). There is a perfusion abnormality in the ^{201}Tl images involving the anterolateral wall of the left ventricle (*LV*). The images obtained after the ^{123}I-*m*IBG injection reveal a markedly larger area of reduced ^{123}I-*m*IBG retention involving the anterolateral wall as well as the distal inferior wall. Polar maps display the disparity of perfusion and neuronal abnormality, reflecting the infarct size and area of denervation. This mismatch between perfusion and ^{123}I-*m*IBG retention is present in almost 80% of patients after acute myocardial infarction and indicates that sympathetic neurons are more sensitive to ischemia than the myocytes [57]. Although reduced ^{11}C-HED retention was found in an experimental model of chronically ischemic hibernating myocardium, the dependency of the ^{11}C-HED retention on resting myocardial blood flow or flow reserve was small in patients with chronic coronary artery disease [58]. LA left atrium, RA right atrium, RV right ventricle

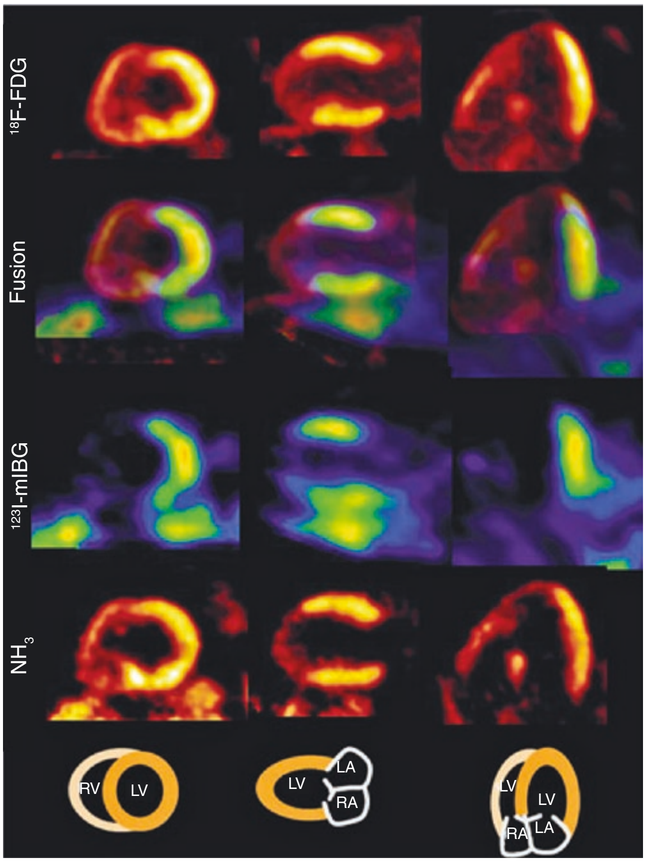

Fig. 11.22 Myocardium as a substrate for ventricular arrhythmias. It has been proposed that denervated but viable myocardium can form a substrate for ventricular arrhythmias after myocardial infarction. The mismatch pattern of innervation and viability has been shown to correlate with abnormal electrophysiologic findings [59–62]. However, its relationship to clinical arrhythmic events remains unclear [59]. The figure demonstrates a detailed assessment of viability, perfusion, and sympathetic innervation by evaluation of fluorodeoxyglucose (^{18}F-FDG) uptake with PET, ^{13}N-ammonia (NH_3) PET, and ^{123}I-*m*IBG SPECT in a patient with a previous anterior myocardial infarction and sustained ventricular tachycardia, being considered for ablation

Atrial and Ventricular Arrhythmias

Atrial fibrillation is the most common tachyarrhythmia in humans. Ablation of atrial fibrillation in the electrophysiology laboratory is becoming the preferred or definitive approach for therapy, supplanting medical therapy, surgery, and observation with or without anticoagulation. In the absence of structural heart disease, it is impossible to predict reliably whether a patient with a first self-terminated episode of atrial fibrillation will progress to permanent atrial fibrillation. ^{123}I-*m*IBG scintigraphy is emerging as a risk-stratification modality that can distinguish which individuals will progress to have permanent atrial fibrillation or permanent atrial fibrillation and congestive heart failure [63]. In 98 consecutive subjects with idiopathic paroxysmal atrial fibrillation and preserved LVEF, the role of cardiac ^{123}I-*m*IBG SPECT in the transition to permanent atrial fibrillation and the occurrence of heart failure were assessed. During a 4-year follow-up period, 35 of the subjects (36%) transitioned to permanent atrial fibrillation. A low ^{123}I-*m*IBG HMR and low LVEF were independent predictors of the transition to permanent atrial fibrillation. Further, a low ^{123}I-*m*IBG HMR, low LVEF, and a high plasma brain natriuretic peptide concentration were independent predictors of the occurrence of heart failure with permanent atrial fibrillation. Sympathetic innervation may play a key role in cardiovascular remodeling, which promotes atrial fibrillation. Figure 11.23 presents three examples of the prognostic use of ^{123}I-*m*IBG SPECT and ECG.

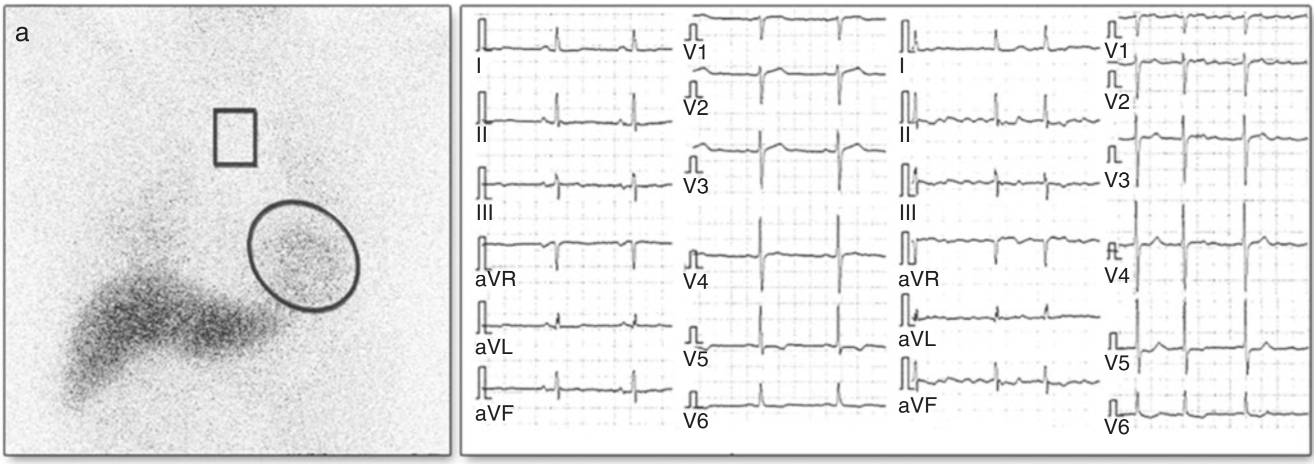

H/M ratio = 2.7

The sinus rhythm → The transit to permanent AF

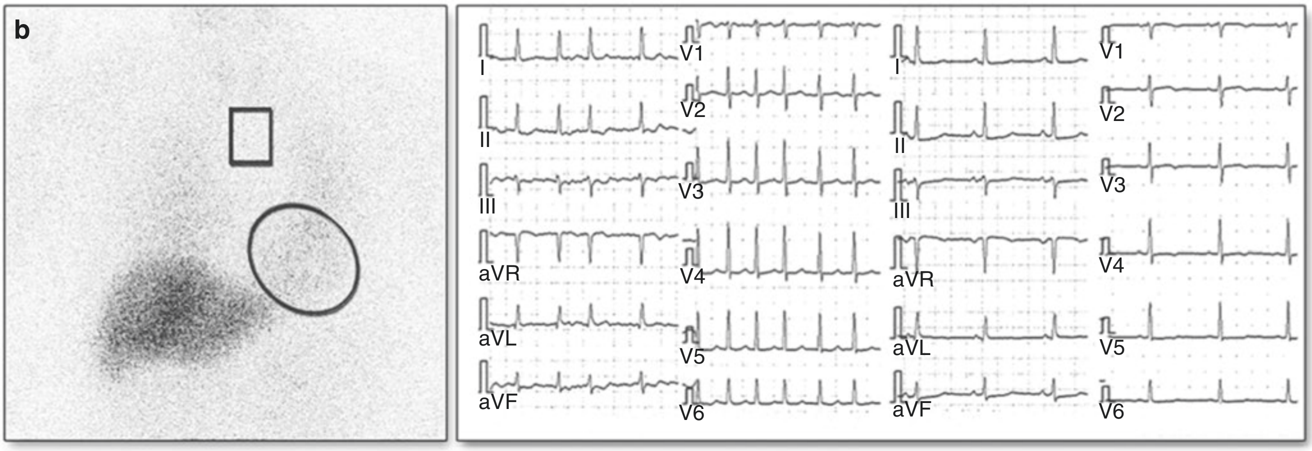

H/M ratio = 2.7

The occurence of HF with AF → The recovery to sinus rhythm

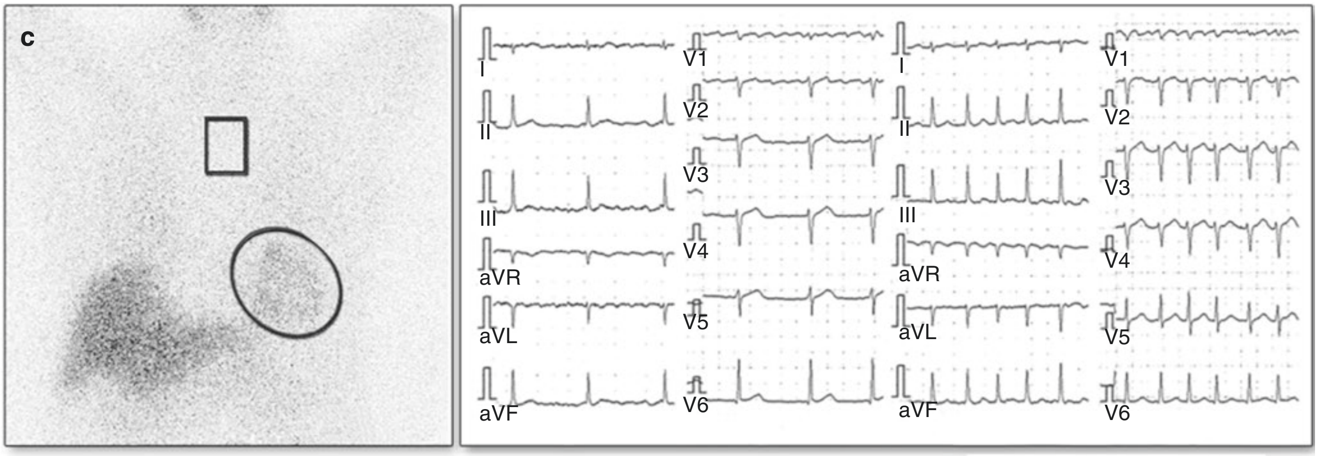

H/M ratio = 2.5

The transit to permanent AF → The occurence of HF with permanent AF

Fig. 11.23 ^{123}I-*m*IBG image examples and electrocardiography (ECG) strips for predicting atrial fibrillation (AF). In these examples of ^{123}I-*m*IBG images and ECG strips, the ovals indicate the region of interest on the heart area (H) and the rectangles indicate the region of interest on mediastinum (M). Cardiac sympathetic nervous system activity was estimated by the value of the heart/mediastinum (H/M) ratio. (**a**) A 78-year-old man with paroxysmal AF had a 2.7 H/M ratio in the ^{123}I-*m*IBG image and transited to permanent AF without the occurrence of heart failure (HF). (**b**) A 68-year-old man with paroxysmal AF had a 2.6 H/M ratio. The HF with AF occurred afterward, but the improvement of HF resulted in recovery to sinus rhythm from AF. (**c**) A 71-year-old man with paroxysmal AF had a 2.5 H/M ratio and transited to permanent AF. The HF occurred afterward, and the AF was perpetuated after the improvement of HF. These patients with paroxysmal AF had significantly lower H/M ratios than normal values (3.3 ± 0.5) (From Akutsu et al. [63]; with permission from Elsevier)

Similarly, experimental and clinical studies have linked presynaptic and postsynaptic sympathetic nervous function and the presence of ventricular arrhythmias [64–66]. Innervation imaging has demonstrated abnormalities in patients with primary arrhythmic cardiac disorders in the absence of structural heart disease, such as right ventricular outflow tract tachycardia (Fig. 11.24), Brugada syndrome, and idiopathic ventricular fibrillation [67–70].

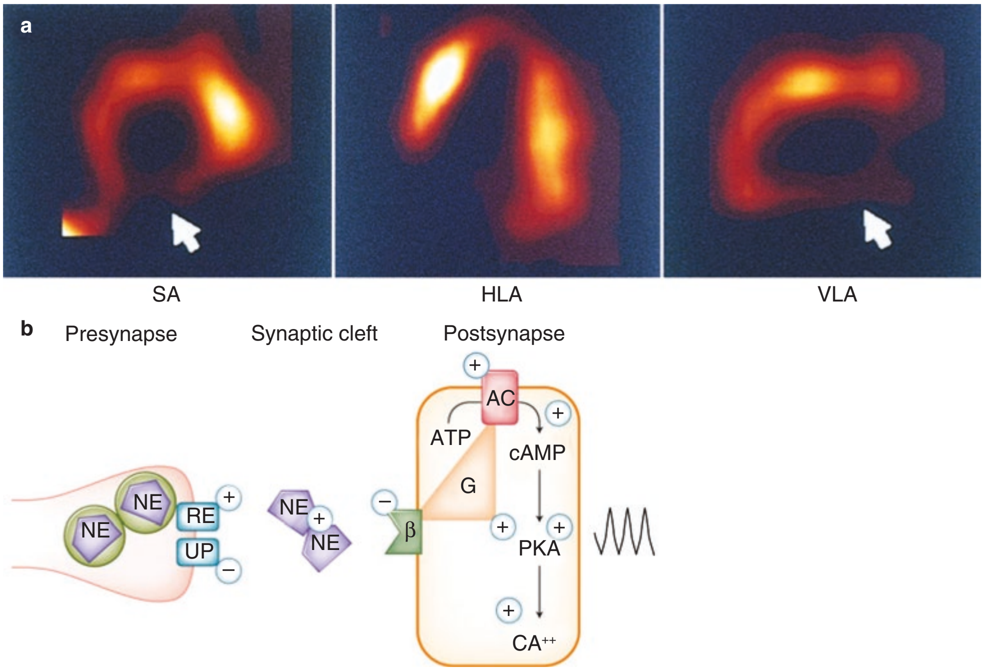

Fig. 11.24 Sympathetic denervation and ventricular arrhythmias. (**a**) ^{123}I-*m*IBG SPECT images were obtained in a 54-year-old man with idiopathic right ventricular outflow tract tachycardia. The tomographic slices are displayed in short-axis (SA), horizontal long-axis (HLA), and vertical long-axis (VLA) views. The ^{123}I-*m*IBG images acquired 4 hours following injection show a marked ^{123}I-*m*IBG retention defect in the midventricular and basal inferior walls (*arrows*), suggesting regional sympathetic denervation. Unfortunately, the right ventricle cannot be imaged by radionuclide techniques because of its thin myocardial walls. (**b**) This schematic display illustrates a proposed pathophysiologic mechanism of tachycardia in patients with idiopathic right ventricular outflow tract tachycardia. Impairment of a catecholamine clearance contributes to reduced clearance of neurotransmitter from the synaptic cleft and, thus, to myocardial catecholamine overexposure. The resulting presynaptic and postsynaptic imbalance is thought to contribute to electrical instability and arrhythmogenesis. Assuming that stimulatory G proteins (G) are upregulated in connection with downregulated β-adrenoceptors, an acute increase in synaptic norepinephrine (NE) concentration would increase cyclic adenosine 3′,5′-monophosphate (cAMP) via activation of adenylyl cyclase (AC). The increase in cAMP will produce a rise in intracellular Ca^{2+} levels by activation of protein kinase A (PKA) and will eventually trigger ventricular tachycardia. ATP adenosine triphosphate, RE release, UP uptake

Figure 11.25 shows the results of a study relating imaging findings and ventricular arrhythmias in patients treated with an implantable cardioverter defibrillator (ICD). ICDs that are capable of ECG recording at the time of arrhythmias provide an opportunity to study the association between ^{123}I-*m*IBG imaging findings and ventricular arrhythmias [70–72]. In this study, Nagahara et al. [72] prospectively followed 53 patients treated with ICD for 15 months after ^{123}I-*m*IBG imaging. Most patients ($n = 39$) had underlying structural heart disease, including nine patients with idiopathic dilated cardiomyopathy and eight patients with ischemic heart disease. The graph shows that patients who had appropriate ICD discharges due to life-threatening ventricular arrhythmias ($n = 21$) or who died of cardiac causes had significantly lower HMRs than the other patients. The value of ^{123}I-*m*IBG imaging in improving the selection of patients for treatment with ICD remains to be established in future trials involving larger numbers of patients who are representative of the common underlying etiologies of heart failure, particularly ischemic heart disease.

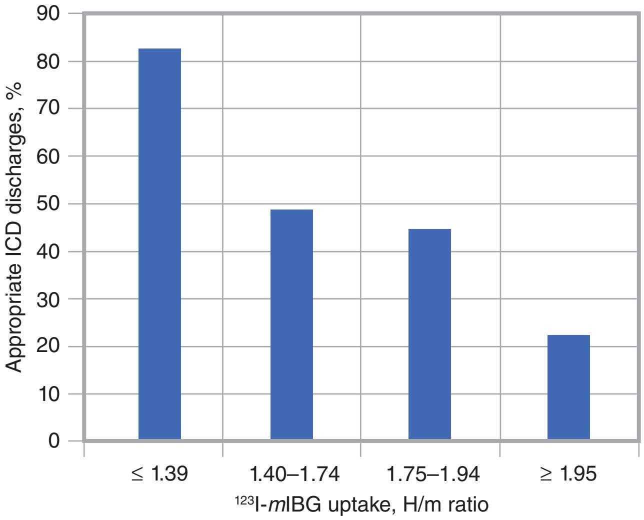

Fig. 11.25 Implantable cardioverter defibrillators (ICDs) for the study of imaging findings and ventricular arrhythmias. Patients who had appropriate ICD discharges due to life-threatening ventricular arrhythmias ($n = 21$) or died of cardiac causes had significantly lower H/M ratios than the other patients. The H/M ratio of 1.95 was the optimal cutoff value that identified arrhythmias (area under the ROC curve, 0.68) independently of many other variables, including LVEF and plasma brain natriuretic peptide (BNP) level. The event rates among quartiles of the H/M ratio are shown. When the H/M ratio was combined with either LVEF or BNP, their sensitivities were 67% and 45%, with specificities of 70% and 94%, respectively, better than those provided by LVEF alone [72]

Diabetes

Heterogeneous denervation is seen in patients with diabetic neuropathy (Fig. 11.26) and has been linked to an increased incidence of sudden cardiac death in patients with diabetic neuropathy of the heart [73]. A correlation has been established between the degree of cardiac denervation and the clinical parameters of autonomic dysfunction [74, 75]. The scintigraphic determination of presynaptic tracer uptake appears to be more sensitive than clinical parameters in detecting early involvement of the heart in diabetic neuropathy, but no prospective data are available defining the prognostic value of neuronal imaging for detection of patients with increased incidence of cardiovascular complications [73, 74, 76–78].

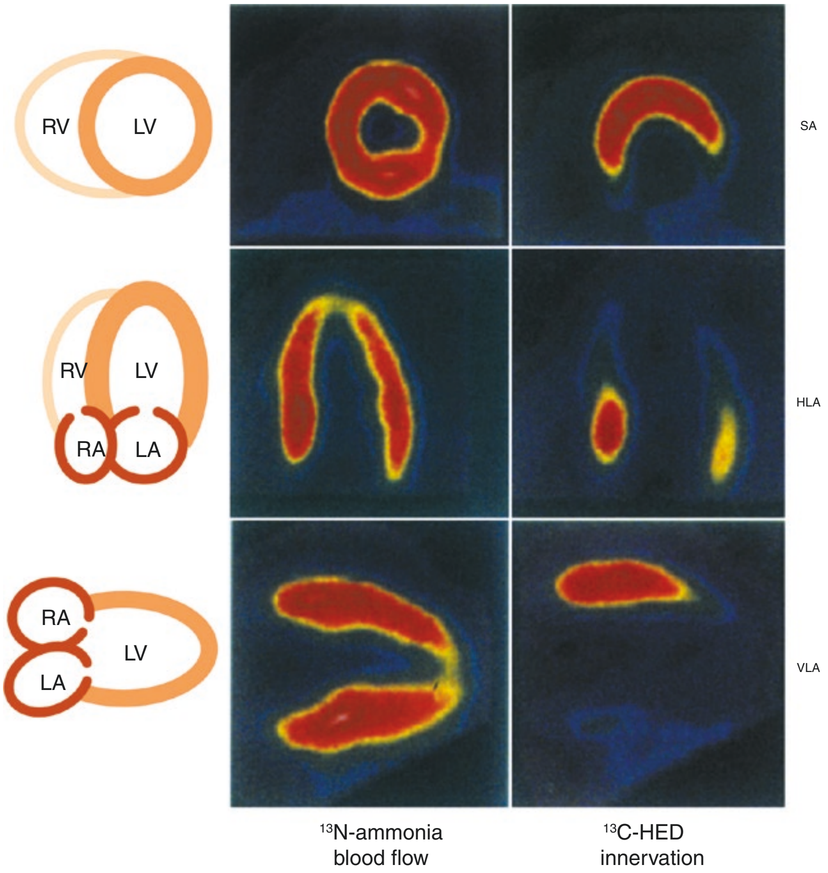

Fig. 11.26 Myocardial neuropathy in diabetes. These PET images were obtained from a patient with advanced diabetic neuropathy as defined by functional testing. Following the injection of ^{11}C-HED, short-axis (SA), horizontal long-axis (HLA), and vertical long-axis (VLA) views were obtained. The regional retention of ^{11}C-HED is compared with the regional perfusion as assessed by ^{13}N-ammonia. There is heterogeneous denervation in patients with diabetic neuropathy. The ^{11}C-HED retention is reduced most prominently in the distal aspects of the anterior wall, apex, and inferior wall of the left ventricle (LV). As the process of neuropathy proceeds, denervation starts at the apex and extends to the basal aspects of the LV. The proximal, anterior, and anterolateral wall segments are most protected from the disease process. This heterogeneity of denervation has been linked to the increased incidence of sudden cardiac death in these patients. LA left atrium, RA right atrium, RV right ventricle

Cardiac Transplantation

Cardiac transplantation represents the best model of cardiac denervation because the neuronal fibers are cut during the transplantation surgery. As time after the cardiac transplantation passes, however, there is evidence for regional reinnervation [25]. Figure 11.27 depicts the reinnervation process occurring in about 40–50% of patients. The reinnervation process does not result in complete reinnervation but shows the regional reappearance of sympathetic nerve terminals. Functional studies have shown that patients with reinnervation show greater heart rate variability, better exercise tolerance, and improved LV function with exercise [80].

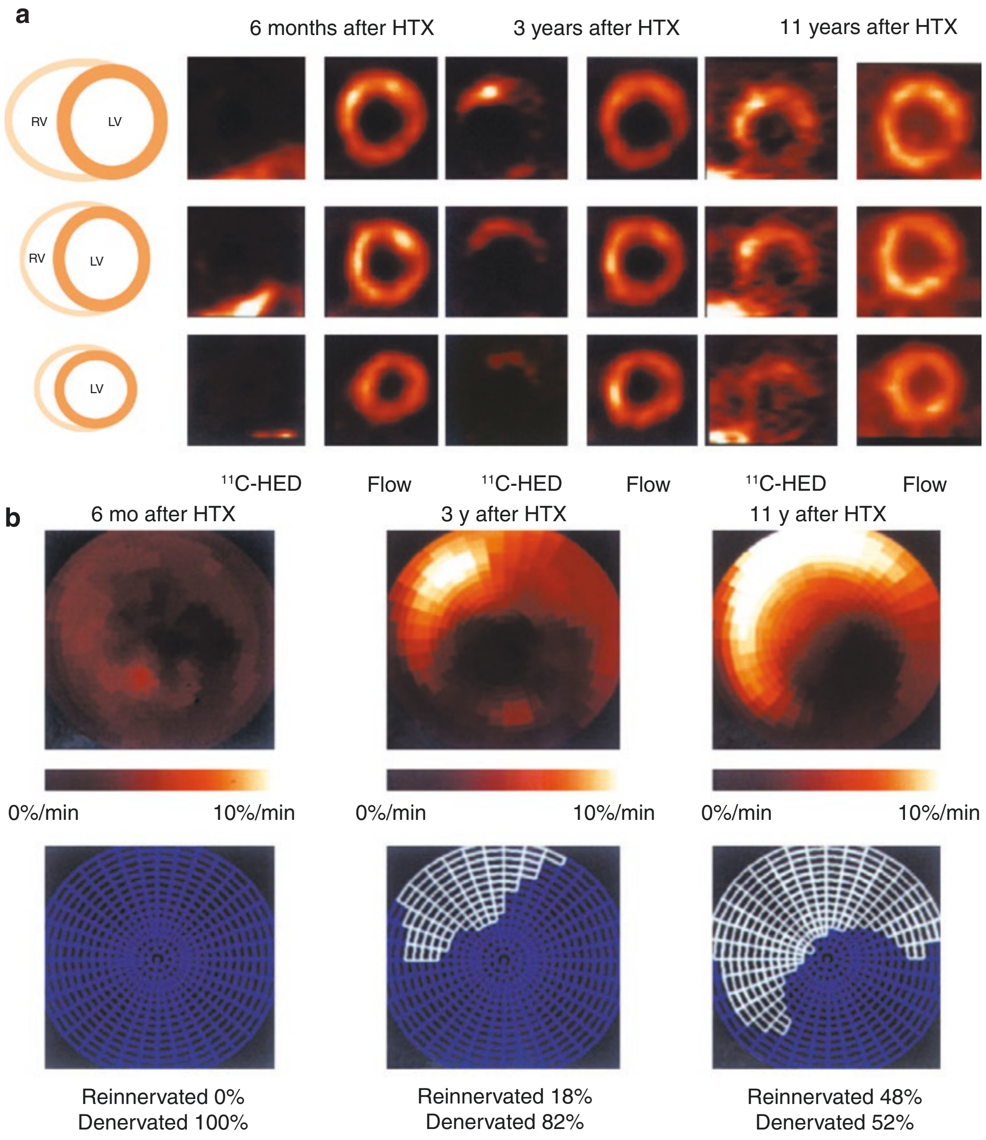

Fig. 11.27 Reinnervation of cardiac allograft. Uptake of radiolabeled catecholamines in the anterior wall, septum, and base of the left ventricle (LV) indicates the reappearance of functioning sympathetic nerve terminals. The pharmacologic integrity of these nerve terminals has been demonstrated by studies of neurotransmitter released following the intracoronary injection of tyramine [79]. A study linking regional tracer uptake with exercise capacity indicates that the reinnervation process is beneficial for the exercise performance of patients following heart transplantation [80]. (**a**) Neuronal imaging with ^{11}C-HED obtained 6 months after heart transplantation (HTX) shows little retention of the tracer in the myocardium 40 minutes after the tracer injection, in comparison to the myocardial perfusion assessed with ^{13}N-ammonia. In a patient studied 3 years after heart transplantation, myocardial perfusion is homogeneous throughout the LV, but the ^{11}C-HED images obtained 40 minutes after injection reveal the reappearance of regional ^{11}C-HED retention in the anteroseptal area of the LV. The area of reinnervation appears larger in a patient studied 11 years after transplantation, but regional denervation remains detectable in inferior aspects of the LV, which display normal perfusion. (**b**) PET–^{11}C-HED polar maps of cardiac transplantation patients at various time points after surgery. Early after transplantation, the retention index is reduced throughout the entire LV myocardium. Using a threshold of 7%/min retention index, no reinnervated area can be detected. At 3 years after transplantation, the anteroseptal areas show reinnervated territories (about 18% of the LV). The PET images obtained 11 years after transplantation show a reinnervated area of 48% of the LV, illustrating the progress of the reinnervation process in the anterior septal wall toward the apex. However, the inferior inferolateral wall remains denervated, as seen in most patients undergoing neuronal imaging late after cardiac transplantation [80–82]. RV right ventricle

References

1. Levy M. Sympathetic-parasympathetic interaction in the heart. In: Kulbertus HE, Franck G, editors. Neurocardiology. New York: Futura; 1988. p. 85–98.
2. Bristow MR, Minobe W, Rasmussen R, Larrabee P, Skerl L, Klein JW, et al. Beta-adrenergic neuroeffector abnormalities in the failing human heart are produced by local rather than systemic mechanisms. J Clin Invest. 1992;89:803–15.
3. Bristow MR, Anderson FL, Port JD, Skerl L, Hershberger RE, Larrabee P, et al. Differences in beta-adrenergic neuroeffector mechanisms in ischemic versus idiopathic dilated cardiomyopathy. Circulation. 1991;84:1024–39.
4. Somsen GA, Verberne HJ, Fleury E, Righetti A. Normal values and within-subject variability of cardiac I-123 MIBG scintigraphy in healthy individuals: implications for clinical studies. J Nucl Cardiol. 2004;11:126–33.
5. Momose M, Tyndale-Hines L, Bengel FM, Schwaiger M. How heterogeneous is the cardiac autonomic innervation? Basic Res Cardiol. 2001;96:539–46.
6. Bannister R, Mathias CJ. Introduction and classification of autonomic disorders. In: Bannister R, Mathias CJ, editors. Autonomic failure. New York: Oxford University Press; 1992. p. 1–12.
7. Milner P, Burnstock G. Neurotransmitters in the autonomic nervous system. In: Korczyn AD, editor. Handbook of autonomic nervous system dysfunction. New York: Marcel Dekker; 1995. p. 5–32.
8. Lipscombe D, Kongsamut S, Tsien RW. Alpha-adrenergic inhibition of sympathetic neurotransmitter release mediated by modulation of N-type calcium-channel gating. Nature. 1989;340:639–42.
9. Toth PT, Bindokas VP, Bleakman D, Colmers WF, Miller RJ. Mechanism of presynaptic inhibition by neuropeptide Y at sympathetic nerve terminals. Nature. 1993;364:635–9.
10. Nicholls JG, Martin AR, Wallace BG. From neuron to brain. 3rd ed. Sinauer: Sunderland; 1992.
11. Langer O, Halldin C. PET and SPECT tracers for mapping the cardiac nervous system. Eur J Nucl Med. 2002;29:416–34.
12. Kline RC, Swanson DP, Wieland DM, Thrall JH, Gross MD, Pitt B, Beierwaltes WH. Myocardial imaging in man with I-123 meta-iodobenzylguanidine. J Nucl Med. 1981;22:129–32.
13. Wieland DM, Rosenspire KC, Hutchins GD, Van Dort M, Rothley JM, Mislankar SG, et al. Neuronal mapping of the heart with 6-[18F]fluorometaraminol. J Med Chem. 1990;33:956–64.
14. Rosenspire KC, Haka MS, Van Dort ME, Jewett DM, Gildersleeve DL, Schwaiger M, Wieland DM. Synthesis and preliminary evaluation of carbon-11-meta-hydroxyephedrine: a false transmitter agent for heart neuronal imaging. J Nucl Med. 1990;31:1328–34.
15. Raffel DM, Corbett JR, del Rosario RB, Gildersleeve DL, Chiao PC, Schwaiger M, Wieland DM. Clinical evaluation of carbon-11-phenylephrine: MAO-sensitive marker of cardiac sympathetic neurons. J Nucl Med. 1996;37:1923–31.
16. Degrado TR, Zalutsky MR, Vaidyanathan G. Uptake mechanisms of meta-[123I]iodobenzylguanidine in isolated rat heart. Nucl Med Biol. 1995;22:1–12.
17. Nakajima K, Taki J, Tonami N, Hisada K. Decreased 123I-MIBG uptake and increased clearance in various cardiac diseases. Nucl Med Commun. 1994;15:317–23.
18. Bengel FM, Barthel P, Matsunari I, Schmidt G, Schwaiger M. Kinetics of 123I-MIBG after acute myocardial infarction and reperfusion therapy. J Nucl Med. 1999;40:904–10.
19. Yamada T, Shimonagata T, Fukunami M, Kumagai K, Ogita H, Hirata A, et al. Comparison of the prognostic value of cardiac iodine-123 metaiodobenzylguanidine imaging and heart rate variability in patients with chronic heart failure: a prospective study. J Am Coll Cardiol. 2003;41:231–8.
20. Patel A, Iskandrian A. MIBG imaging. J Nucl Cardiol. 2002;9:75–94.
21. Farahati J, Bier D, Scheubeck M, Lassmann M, Schelper LF, Grelle I, et al. Effect of specific activity on cardiac uptake of iodine-123-MIBG. J Nucl Med. 1997;38:447–51.
22. DeGrado TR, Zalutsky MR, Coleman RE, Vaidyanathan G. Effects of specific activity on meta-[(131)I]iodobenzylguanidine kinetics in isolated rat heart. Nucl Med Biol. 1998;25:59–64.
23. Verberne HJ, Brewster LM, Somsen GA, van Eck-Smit BL. Prognostic value of myocardial 123I-metaiodobenzylguanidine (MIBG) parameters in patients with heart failure: a systematic review. Eur Heart J. 2008;29:1147–59.
24. Schwaiger M, Kalff V, Rosenspire K, Haka MS, Molina E, Hutchins GD, et al. Noninvasive evaluation of sympathetic nervous system in human heart by positron emission tomography. Circulation. 1990;82:457–64.
25. Schwaiger M, Hutchins GD, Kalff V, Rosenspire K, Haka MS, Mallette S, et al. Evidence for regional catecholamine uptake and storage sites in the transplanted human heart by positron emission tomography. J Clin Invest. 1991;87:1681–90.
26. Münch G, Nguyen NT, Nekolla S, Ziegler S, Muzik O, Chakraborty P, et al. Evaluation of sympathetic nerve terminals with [(11)C]epinephrine and [(11)D]hydroxyephedrine and positron emission tomography. Circulation. 2000;101:516–23.
27. Delforge J, Syrota A, Lançon JP, Nakajima K, Loc'h C, Janier M, et al. Cardiac beta-adrenergic receptor density measured in vivo using PET, CGP 12177, and a new graphical method. J Nucl Med. 1991;32:739–48. [Erratum in J Nucl Med. 1994;35:921].
28. Hartmann F, Ziegler S, Nekolla S, Hadamitzky M, Seyfarth M, Richardt G, Schwaiger M. Regional patterns of myocardial sympathetic denervation in dilated cardiomyopathy: an analysis using carbon-11 hydroxyephedrine and positron emission tomography. Heart. 1999;81:262–70.
29. Caldwell JH, Link JM, Levy WC, et al. Evidence for pre- to postsynaptic mismatch of the cardiac sympathetic nervous system in ischemic congestive heart failure. J Nucl Med. 2008;49:234–41.
30. Narula J, Gerson M, Thomas GS, Cerqueira MD, Jacobson AF. I-123 *m*IBG imaging for prediction of mortality and potentially fatal events in heart failure: the ADMIRE-HFX study. J Nucl Med. 2015;56:1011–8.
31. Agostini D, Ananthasubramaniam K, Chandna H, et al. Prognostic usefulness of planar 123I-MIBG scintigraphic images of myocardial sympathetic innervation in congestive heart failure: Follow-up data from ADMIRE-HF. J Nucl Cardiol 2019. https://doi.org/10.1007/s12350-019-01859-w.
32. Nakata T, Nakajima K, Yamashina S, Yamada T, Momose M, Kasama S, et al. A pooled analysis of multicenter cohort studies of (123)I-mIBG imaging of sympathetic innervation for assessment of long-term prognosis in heart failure. JACC Cardiovasc Imaging. 2013;6:772–84.
33. Chen J, Folks RD, Verdes L, Manatunga DN, Jacobson AF, Garcia EV. Quantitative I123 mIBG SPECT in differentiating abnormal and normal mIBG myocardial uptake. J Nucl Cardiol. 2012;19:92–9.
34. Bax JJ, Kraft O, Buxton AE, Fjeld JG, Parízek P, Agostini D, et al. 123 I-mIBG scintigraphy to predict inducibility of ventricular arrhythmias on cardiac electrophysiology testing: a prospective multicenter pilot study. Circ Cardiovasc Imaging. 2008;1:131–40.
35. Boogers MJ, Borleffs CJ, Henneman MM, van Bommel RJ, van Ramshorst J, Boersma E, et al. Cardiac sympathetic denervation assessed with 123-iodine metaiodobenzylguanidine imaging predicts ventricular arrhythmias in implantable cardioverter-defibrillator patients. J Am Coll Cardiol. 2010;55:2769–77.
36. Marshall A, Cheetham A, George RS, Mason M, Kelion AD. Cardiac iodine-123 metaiodobenzylguanidine imaging pre-

dicts ventricular arrhythmia in heart failure patients receiving an implantable cardioverter-defibrillator for primary prevention. Heart. 2012;98:1359–65.

37. Ketchum ES, Jacobson AF, Caldwell JH, Senior R, Cerqueira MD, Thomas GS, et al. Selective improvement in Seattle heart failure model risk stratification using Iodine-123 meta-iodobenzylguanidine imaging. J Nucl Cardiol. 2012;19:1007–16.
38. Jain KK, Hauptman PJ, Spertus JA, Kennedy KF, Bateman TM, Jacobson AF, Stolker JM. Incremental utility of iodine-123 meta-Iodobenzylguanidine imaging beyond established heart failure risk models. J Card Fail. 2014;20:577–83.
39. Nakajima K, Nakata T, Matsuo S, Jacobson AF. Creation of mortality risk charts using 123I meta-iodobenzylguanidine heart-to-mediastinum ratio in patients with heart failure: 2- and 5-year risk models. Eur Heart J Cardiovasc Imaging. 2016;17:1138–45.
40. Nakajima K, Nakata T, Doi T, Kadokami T, Matsuo S, Konno T, et al. Validation of 2-year 123I-meta-iodobenzylguanidine-based cardiac mortality risk model in chronic heart failure. Eur Heart J Cardiovasc Imaging. 2018;19:749–56.
41. Link JM, Caldwell JH. Diagnostic and prognostic imaging of the cardiac sympathetic nervous system. Nat Clin Pract Cardiovasc Med. 2008;5(Suppl 2):S79–86.
42. Fallavollita JA, Heavey BM, Luisi AJ Jr, Michalek SM, Baldwa S, Mashtare TL, et al. Regional myocardial sympathetic denervation predicts the risk of sudden cardiac arrest in ischemic cardiomyopathy. J Am Coll Cardiol. 2014;63:141–9.
43. Harms HJ, Huisman MC, Rijnierse MT, Greuter H, Hsieh YL, de Haan S, et al. Noninvasive quantification of myocardial 11C-meta-hydroxyephedrine kinetics. J Nucl Med. 2016;57:1376–81.
44. Harms HJ, Lubberink M, de Haan S, Knaapen P, Huisman MC, Schuit RC, et al. Use of a single 11C-meta-hydroxyephedrine scan for assessing flow-innervation mismatches in patients with ischemic cardiomyopathy. J Nucl Med. 2015;56:1706–11.
45. Bengel FM, Schwaiger M. Assessment of cardiac sympathetic neuronal function using PET imaging. J Nucl Cardiol. 2004;11:603–16.
46. Thackeray JT, Bengel FM. Assessment of cardiac autonomic neuronal function using PET imaging. J Nucl Cardiol. 2013;20:150–65.
47. Tokuda Y, Sakakibara M, Yoshinaga K, Yamada S, Kamiya K, Asakawa N, et al. Early therapeutic effects of adaptive servo-ventilation on cardiac sympathetic nervous function in patients with heart failure evaluated using a combination of ^{11}C-HED PET and ^{123}I-MIBG SPECT. J Nucl Cardiol. 2019;26:1079–89.
48. Aikawa T, Naya M, Obara M, Oyama-Manabe N, Manabe O, Magota K, et al. Regional interaction between myocardial sympathetic denervation, contractile dysfunction, and fibrosis in heart failure with preserved ejection fraction: ^{11}C-hydroxyephedrine PET study. Eur J Nucl Med Mol Imaging. 2017;44:1897–905.
49. Sinusas AJ, Lazewatsky J, Brunetti J, Heller G, Srivastava A, Liu YH, et al. Biodistribution and radiation dosimetry of LMI1195: first-in-human study of a novel 18F-labeled tracer for imaging myocardial innervation. J Nucl Med. 2014;55:1445–51.
50. Jung YW, Jang KS, Gu G, Koeppe RA, Sherman PS, Quesada CA, Raffel DM. [^{18}F]Fluoro-hydroxyphenethylguanidines: efficient synthesis and comparison of two structural isomers as radiotracers of cardiac sympathetic innervation. ACS Chem Neurosci. 2017;8:1530–42.
51. Zhou Y, Zhou W, Folks RD, Manatunga DN, Jacobson AF, Bax JJ, et al. I-123 mIBG and Tc-99m myocardial SPECT imaging to predict inducibility of ventricular arrhythmia on electrophysiology testing: a retrospective analysis. J Nucl Cardiol. 2014;21:913–20.
52. Klein T, Abdulghani M, Smith M, Huang R, Asoglu R, Remo BF, et al. Three-dimensional 123I-meta-iodobenzylguanidine cardiac innervation maps to assess substrate and successful ablation sites for ventricular tachycardia: feasibility study for a novel paradigm of innervation imaging. Circ Arrhythm Electrophysiol. 2015;8:583–91.
53. Lautamaki R, Sasano T, Higuchi T, Nekolla SG, Lardo AC, Holt DP, et al. Multiparametric molecular imaging provides mechanistic insights into sympathetic innervation impairment in the viable infarct border zone. J Nucl Med. 2015;56:457–63.
54. Pina IL, Carson P, Lindenfeld J, Archambault T, Jacobson AF. Persistence of 123I-mIBG prognostic capability in relation to medical therapy in heart failure (from the ADMIRE-HF trial). Am J Cardiol. 2017;119:434–9.
55. Jacobson AF, White S, Travin MI, Tseng C. Impact of concomitant medication use on myocardial ^{123}I-*m*IBG imaging results in patients with heart failure. Nucl Med Commun. 2017;38:141–8.
56. Allman KC, Wieland DM, Muzik O, Degrado TR, Wolfe ER Jr, Schwaiger M. Carbon-11 hydroxyephedrine with positron emission tomography for serial assessment of cardiac adrenergic neuronal function after acute myocardial infarction in humans. J Am Coll Cardiol. 1993;22:368–75.
57. Matsunari I, Schricke U, Bengel FM, Haase HU, Barthel P, Schmidt G, et al. Extent of cardiac sympathetic neuronal damage is determined by the area of ischemia in patients with acute coronary syndromes. Circulation. 2000;101:2579–85.
58. Fricke E, Fricke H, Eckert S, Zijlstra S, Weise R, Lindner O, et al. Myocardial sympathetic innervation in patients with chronic coronary artery disease: is reduction in coronary flow reserve correlated with sympathetic denervation? Eur J Nucl Med Mol Imaging. 2007;34:206–11.
59. Yukinaka M, Nomura M, Ito S, Nakaya Y. Mismatch between myocardial accumulation of 123I-MIBG and 99mTc-MIBI and late ventricular potentials in patients after myocardial infarction: association with the development of ventricular arrhythmias. Am Heart J. 1998;136:859–67.
60. Simões MV, Barthel P, Matsunari I, Nekolla SG, Schömig A, Schwaiger M, et al. Presence of sympathetically denervated but viable myocardium and its electrophysiologic correlates after early revascularised, acute myocardial infarction. Eur Heart J. 2004;25:551–7.
61. Calkins H, Allman K, Bolling S, Kirsch M, Wieland D, Morady F, Schwaiger M. Correlation between scintigraphic evidence of regional sympathetic neuronal dysfunction and ventricular refractoriness in the human heart. Circulation. 1993;88:172–9.
62. Sasano T, Abraham MR, Chang KC, Ashikaga H, Mills KJ, Holt DP, et al. Abnormal sympathetic innervation of viable myocardium and the substrate of ventricular tachycardia after myocardial infarction. J Am Coll Cardiol. 2008;51:2266–75.
63. Akutsu Y, Kaneko K, Kodama Y, Li HL, Suyama J, Shinozuka A, et al. Iodine-123 imaging for predicting the development of atrial fibrillation. JACC Cardiovasc Imaging. 2011;4:78–86.
64. Schwartz PJ. The autonomic nervous system and sudden death. Eur Heart J. 1998;19:F72–80.
65. Meredith IT, Broughton A, Jennings GL, Esler MD. Evidence of a selective increase in cardiac sympathetic activity in patients with sustained ventricular arrhythmias. N Engl J Med. 1991;325:618–24.
66. Rubart M, Zipes DP. Mechanisms of sudden cardiac death. J Clin Invest. 2005;115:2305–15.
67. Wichter T, Schäfers M, Rhodes CG, Borggrefe M, Lerch H, Lammertsma AA, et al. Abnormalities of cardiac sympathetic innervation in arrhythmogenic right ventricular cardiomyopathy: quantitative assessment of presynaptic norepinephrine reuptake and postsynaptic beta-adrenergic receptor density with positron emission tomography. Circulation. 2000;101:1552–8.
68. Schäfers M, Lerch H, Wichter T, Rhodes CG, Lammertsma AA, Borggrefe M, et al. Cardiac sympathetic innervation in patients with idiopathic right ventricular outflow tract tachycardia. J Am Coll Cardiol. 1998;32:181–6.

69. Kies P, Wichter T, Schäfers M, Paul M, Schäfers KP, Eckardt L, et al. Abnormal myocardial presynaptic norepinephrine recycling in patients with Brugada syndrome. Circulation. 2004;110:3017–22.
70. Paul M, Schäfers M, Kies P, Acil T, Schäfers K, Breithardt G, et al. Impact of sympathetic innervation on recurrent life-threatening arrhythmias in the follow-up of patients with idiopathic ventricular fibrillation. Eur J Nucl Med Mol Imaging. 2006;33:866–70.
71. Arora R, Ferrick KJ, Nakata T, Kaplan RC, Rozengarten M, Latif F, et al. I-123 MIBG imaging and heart rate variability analysis to predict the need for an implantable cardioverter defibrillator. J Nucl Cardiol. 2003;10:121–31.
72. Nagahara D, Nakata T, Hashimoto A, Wakabayashi T, Kyuma M, Noda R, et al. Predicting the need for an implantable cardioverter defibrillator using cardiac metaiodobenzylguanidine activity together with plasma natriuretic peptide concentration or left ventricular function. J Nucl Med. 2008;49:225–33.
73. Langen KJ, Ziegler D, Weise F, Piolot R, Boy C, Hübinger A, et al. Evaluation of QT interval length, QT dispersion and myocardial m-iodobenzylguanidine uptake in insulin-dependent diabetic patients with and without autonomic neuropathy. Clin Sci (Lond). 1997;93:325–33.
74. Stevens MJ, Raffel DM, Allman KC, Dayanikli F, Ficaro E, Sandford T, et al. Cardiac sympathetic dysinnervation in diabetes: implications for enhanced cardiovascular risk. Circulation. 1998;98:961–8.
75. Pop-Busui R, Kirkwood I, Schmid H, Marinescu V, Schroeder J, Larkin D, et al. Sympathetic dysfunction in type 1 diabetes: association with impaired myocardial blood flow reserve and diastolic dysfunction. J Am Coll Cardiol. 2004;44:2368–74.
76. Allman KC, Stevens MJ, Wieland DM, Hutchins GD, Wolfe ER Jr, Greene DA, Schwaiger M. Noninvasive assessment of cardiac diabetic neuropathy by carbon-11 hydroxyephedrine and positron emission tomography. J Am Coll Cardiol. 1993;22:1425–32.
77. Ziegler D, Weise F, Langen KJ, Piolot R, Boy C, Hübinger A, et al. Effect of glycaemic control on myocardial sympathetic innervation assessed by [123I]metaiodobenzylguanidine scintigraphy: a 4-year prospective study in IDDM patients. Diabetologia. 1998;41:443–51.
78. Wei K, Dorian P, Newman D, Langer A. Association between QT dispersion and autonomic dysfunction in patients with diabetes mellitus. J Am Coll Cardiol. 1995;26:859–63.
79. Odaka K, von Scheidt W, Ziegler SI, Ueberfuhr P, Nekolla SG, Reichart B, et al. Reappearance of cardiac presynaptic sympathetic nerve terminals in the transplanted heart: correlation between PET using (11) C-hydroxyephedrine and invasively measured norepinephrine release. J Nucl Med. 2001;42:1011–6.
80. Bengel FM, Ueberfuhr P, Schiepel N, Nekolla SG, Reichart B, Schwaiger M. Effect of sympathetic reinnervation on cardiac performance after heart transplantation. N Engl J Med. 2001;345:731–8.
81. De Marco T, Dae M, Yuen-Green MS, Kumar S, Sudhir K, Keith F, et al. Iodine-123 metaiodobenzylguanidine scintigraphic assessment of the transplanted human heart: evidence for late reinnervation. J Am Coll Cardiol. 1995;25:927–31.
82. Estorch M, Campreciós M, Flotats A, Marí C, Bernà L, Catafau AM, et al. Sympathetic reinnervation of cardiac allografts evaluated by 123I-MIBG imaging. J Nucl Med. 1999;40:911–6.